Simulations of minor mergers. I. General properties of thick disks

Villalobos, Álvaro; Helmi, Amina

Published in:
Monthly Notices of the Royal Astronomical Society

DOI:
10.1111/j.1365-2966.2008.13979.x

Publication date:
2008

Mon. Not. R. Astron. Soc. **391,** 1806–1827 (2008) doi:10.1111/j.1365-2966.2008.13979.x

Simulations of minor mergers – I. General properties of thick discs

Álvaro Villalobos⋆ and Amina Helmi⋆

Kapteyn Astronomical Institute, University of Groningen, PO Box 800, 9700 AV Groningen, The Netherlands

Accepted 2008 September 18. Received 2008 September 17; in original form 2008 March 14

ABSTRACT

We present simulations of the formation of thick discs via the accretion of two-component satellites onto a pre-existing thin disc. Our goal is to establish the detailed characteristics of the thick discs obtained in this way, as well as their dependence on the initial orbital and internal properties of the accreted objects. We find that mergers with 10–20 per cent mass of the host lead to the formation of thick discs whose characteristics are similar, both in morphology as in kinematics, to those observed. Despite the relatively large mass ratios, the host discs are not fully destroyed by the infalling satellites: a remaining kinematically cold and thin component containing ∼15–25 per cent of the mass can be identified, which is embedded in a hotter and thicker disc. This may for example, explain the existence of a very old thin disc stars in the Milky Way. The final scaleheights of the discs depend both on the initial inclination and properties of the merger, but the fraction of satellite stellar particles at ∼4 scaleheights directly measures the mass ratio between the satellite and host galaxy. Our thick discs typically show boxy isophotes at very low surface brightness levels (>6 mag below their peak value). Kinematically, the velocity ellipsoids of the simulated thick discs are similar to that of the Galactic thick disc at the solar radius. The trend of σ_Z/σ_R with radius is found to be a very good discriminant of the initial inclination of the accreted satellite. In the Milky Way, the possible existence of a vertical gradient in the rotational velocity of the thick disc as well as the observed value of σ_Z/σ_R at the solar vicinity appear to favour the formation of the thick disc by a merger with either low or intermediate orbital inclination.

Key words: Galaxy: disc – Galaxy: formation – Galaxy: kinematics and dynamics – galaxies: formation – galaxies: kinematics and dynamics – galaxies: structure.

1 INTRODUCTION

The different components of disc galaxies contain key information about various stages of the formation history of these systems. In this sense, one of the most significant components for studying signatures of galaxy formation are the thick discs because they contain imprints of the state of early discs and their interaction with the galactic environment (Freeman & Bland-Hawthorn 2002).

Until now thick discs have been detected in S0 galaxies (Burstein 1979; Tsikoudi 1979), in the Milky Way (Gilmore & Reid 1983) and in many other spirals (van der Kruit & Searle 1981a,b; Jensen & Thuan 1982; van Dokkum et al. 1994; Morrison et al. 1997; Pohlen et al. 2000; Dalcanton & Bernstein 2002, hereafter DB02; Yoachim & Dalcanton 2006, and references therein). As such, thick discs appear to be a rather ubiquitous structural component of galaxies.

Historically, there have been two types of scenario proposed to explain the formation of thick discs: (i) 'dissipational' and (ii) 'predominantly dissipationless' models. In the first case, thick-disc stars are formed during the dissipational collapse of gas with a large scaleheight, after the halo has formed and before the thin disc has completely developed. A variant of this model, more in line with modern cosmology, is given by Brook et al. (2004,2005) and consists of the formation of the thick disc in an epoch of multiple mergers of gas-rich building blocks. In this class of models, one may expect a smooth transition between properties of the thin and thick discs (Eggen, Lynden-Bell & Sandage 1962; Gilmore & Wyse 1986; Norris & Ryan 1991; Burkert, Truran & Hensler 1992; Pardi, Ferrini & Matteucci 1995; Fuhrmann 2004). Evidence of such a process at work may be the chain and clumpy galaxies observed at high redshift by Elmegreen & Elmegreen (2006), which have also been suggested to be the progenitors of thick discs (e.g. Bournaud, Elmegreen & Elmegreen 2007a). In the 'predominantly dissipationless' models the thick disc stars were either (1) vertically 'heated' from a pre-existent thin disc during a (significant) minor merger (Quinn, Hernquist & Fullagar 1993; Mihos et al. 1995; Robin et al. 1996; Walker, Mihos & Hernquist 1996, hereafter WMH96; Velázquez & White 1999, hereafter VW99; Aguerri, Balcells & Peletier 2001; Chen & the SDSS Collaboration 2001);

⋆E-mail: villalobos@astro.rug.nl (ÁV);ahelmi@astro.rug.nl (AH)

(2) directly deposited at large scaleheights as tidally stripped debris during the accretion of smaller satellite galaxies (Bekki & Chiba 2001; Gilmore, Wyse & Norris 2002; Abadi et al. 2003; Martin et al. 2004; Navarro, Helmi & Freeman 2004; Helmi et al. 2006) or (3) the product of the dissolution of massive thin-disc clusters with small radii and large velocity dispersions (Kroupa 2002). The first and third models have in common the presence of a pre-existing disc component. In this second class of models, the thick disc may be characterized as a completely foreign component.

Models involving either one or more minor mergers – including the case of gas-rich accretion proposed by Brook et al. – are natural in the context of current theories of hierarchical structure formation (e.g. Kazantzidis et al. 2007). Such models are also supported by modern studies of both kinematical and chemical properties of the thick discs in the Milky Way and in external galaxies (Mould 2005; Seth, Dalcanton & de Jong 2005; Yoachim & Dalcanton 2005, 2006). The observed lack of vertical colour and chemical gradients, as well as the presence of counter-rotating discs, favours scenarios in which thin and thick discs formed as separate entities. However, it is unclear to what extent such models reproduce the detailed properties of observed thick discs. For example, in the dissipationless minor merger scenario, the thick disc should contain stars from both the heated thin disc and the accreted satellite. What fraction of the stars comes from each constituent? If they are mostly satellite debris, one may expect a significantly metal-poor thick disc, which appears to be inconsistent with the observations reported in e.g. Mould (2005).

It is the lack of very detailed predictions that motivates us to revisit the problem of thick disc formation. In this paper, we explore the hypothesis of the heating of a pre-existing thin disc by a single minor merger. In the scenario we envisage a new thin disc component would form from the accretion of cold gas after the merger has taken place. However, here we only study the global properties of the final merger product. In a follow-up paper we will focus on its phase-space structure with the aim of making a detailed comparison to the thick disc in the solar neighbourhood, and eventually to uncover the debris from the object that may have triggered its formation (Villalobos & Helmi, in preparation). It is important to note that we shall neglect the effect of gas on the properties of the remnant thick disc for the moment. This simplification should be borne in mind, in particular since the structure of minor merger remnants may be different, as suggested by Naab, Jesseit & Burkert (2006) and Younger et al. (2008).

Significant work has been carried out in the past to model the disc heating process by a minor merger from the numerical point of view, starting from Quinn & Goodman (1986, hereafter QG86), Quinn et al. (1993, hereafter QHF93), Mihos et al. (1995), WMH96, Huang & Carlberg (1997, hereafter HC97), Sellwood, Nelson & Tremaine (1998), VW99 and more recently Kazantzidis et al. (2007), and simultaneously with this work Read et al. (2008). These papers have essentially shown that it is relatively easy to produce thick discs whose general properties are consistent with those observed. However, we believe there is still room for improvement, both in the initial conditions used to model this process, as well as in the degree of detail necessary for comparisons to the latest observations of thick discs.

Besides the work mentioned above, in recent years several authors have studied minor mergers with a number of different goals (other than the formation of thick discs). These include for example, studies of the merger remnants produced by encounters between disc galaxies (as a way of producing a bulge-dominated system e.g. Naab & Burkert 2003; Jesseit, Naab & Burkert 2005; Naab & Trujillo 2006). More recently, also the effects of gas, star formation and feedback have been taken into account (Bournaud, Jog & Combes 2005; Naab, Jesseit & Burkert 2006; di Matteo et al. 2007; Cox et al. 2008). The effects of repeated minor mergers have been considered in e.g. Bournaud, Jog & Combes (2007b) and Kazantzidis et al. (2007).

The space of initial conditions to tackle the formation of the thick disc via minor mergers is very large, and it is not desirable to probe it randomly. We have therefore made the following physically motivated choices. (i) We model the formation of thick discs at two different redshifts, by scaling the properties of the host galaxy and accreted satellite according to cosmological models, as in Mo, Mao & White (1998). (ii) We consider the accretion of relatively massive satellites (10 or 20 per cent mass ratios), embedded in dark matter (DM) haloes, and with stellar distributions that are initially either spherical (and on the fundamental plane of dE+dSphs galaxies) or discy. (iii) The satellites are released much farther away from the host disc compared to previous studies, and their orbits are consistent with those of infalling substructures in cosmological simulations (e.g. Benson 2005).

The outline of this paper is the following: In Section 2 we describe in detail the numerical procedure used to build self-consistently the different components of both the host galaxy and satellites including our choices for the numerical parameters and the orbital parameters of the satellites. Section 3 describes the outcome of the simulations, focusing on the final properties of thick discs and the evolution of satellites. In Section 4 we present a discussion and limitations of our approach. In Section 5 we summarize the main results.

2 SETTING UP THE SIMULATIONS

In this section, we describe in broad terms the procedure adopted to model the host disc galaxy and the (to be accreted) satellite. We refer the interested reader to Appendix A for more details. We consider two configurations: a merger with a host whose properties resemble the Milky Way today (our '$z = 0$' experiment), and a merger with a smaller host disc galaxy (this is our '$z = 1$' experiment). The '$z = 0$' configuration has been often used in the past in the same context (QG86; QHF93; WMH96; HC97; VW99; Aguerri, Balcells & Peletier 2001; Font et al. 2001; Ardi, Tsuchiya & Burkert 2003; Hayashi & Chiba 2006). In the '$z = 1$' configuration both the host system and the satellite's properties are scaled to those expected at $z = 1$ according to the model of Mo et al. (1998). In this case, the aim is to simulate the merger event that might have given rise to the Milky Way thick disc. In this configuration the mass of the present-day thick disc of the Milky Way is roughly equal to the combined mass of the host disc galaxy and the stellar component of the satellite.

In this section we also describe the orbital parameters of the various experiments. Furthermore, we explain the choices made for the numerical parameters employed in our simulations, and describe the global stability of the system.

2.1 Main disc galaxy

We model the main disc galaxy as a self-consistent two-component system, containing a Navarro, Frenk & White (1997, hereafter NFW) DM halo and a stellar disc. The dark halo is adiabatically contracted in response to the formation of a stellar disc in its central part (Blumenthal et al. 1986; Mo et al. 1998). The disc component is constructed following the procedure outlined by Hernquist (1993)

Table 1. Properties of host disc galaxies.

	'$z = 0$'	'$z = 1$'	
NFW halo			
Virial mass, $M_{\rm vir}$	10^{12}	5.07×10^{11}	($M_\odot$)
Virial radius, $R_{\rm vir}$	258.91	122.22	(kpc)
Concentration, c	13.12	6.56	
Circular velocity, $V_{\rm c}(R_{\rm vir})$	129.17	133.87	(km s^{-1})
$N_{\rm H}$	500 000	500 000	
Softening, $\epsilon_{\rm halo}$	0.35	0.41	(kpc)
Disc			
Disc mass, $M_{\rm disc}$	2.8×10^{10}	1.2×10^{10}	($M_\odot$)
Scalelength, $R_{\rm D}$	3.5	1.65	(kpc)
Scaleheight, $\mathcal{Z}_0$	0.35	0.165	(kpc)
Toomre $Q(R = 2.4R_{\rm D})$	2.0	2.0	
$N_{\rm D}$	100 000	100 000	
Softening, $\epsilon_{\rm disc}$	0.05	0.012	(kpc)

and QHF93, and follows a density profile of the form

$$\rho_{\rm d}(R, \mathcal{Z}) = \frac{M_{\rm d}}{8\pi R_{\rm D}^2 \mathcal{Z}_0} \exp\left(-\frac{R}{R_{\rm D}}\right) \mathrm{sech}^2\left(\frac{\mathcal{Z}}{2\mathcal{Z}_0}\right), \quad (1)$$

where $M_{\rm d}$ is the disc mass, $R_{\rm D}$ is the exponential scalelength and $\mathcal{Z}_0$ is the exponential[1] scaleheight.

Following Mo et al. (1998), the ratios $M_{\rm halo}/M_{\rm disc}$ and $R_{\rm vir}/R_{\rm D}$ have been kept nearly constant for all redshifts. The scaleheight $\mathcal{Z}_0$ has been kept as $0.1R_{\rm D}$ according to observations of external galaxies (Kregel, van der Kruit & de Grijs 2002). This has also been assumed in our '$z = 1$' experiments. By keeping this ratio constant, the way in which the mass and dimensions of the disc component scale with redshift is simplified, since it follows the same scaling with redshift as the halo within which it is embedded. The chosen values for the parameters of the main disc galaxy are listed in Table 1 for our '$z = 0$' and '$z = 1$' experiments.

2.2 Satellite galaxies

The satellite galaxies are designed self-consistently with both DM and stellar components. The dark halo follows a NFW density profile, and the initialization procedure is identical to that for the host system.

We consider two possible stellar distributions: an exponential disc and a spherical Hernquist bulge. In this case, the density is given by (Hernquist 1990)

$$\rho_{\rm b}(r) = \frac{M_{\rm b}}{2\pi} \frac{a_{\rm b}}{r(r + a_{\rm b})^3}, \quad (2)$$

where $M_{\rm b}$ is the bulge mass and $a_{\rm b}$ is the scale radius.

Both types of satellites satisfy $M_{\rm total,sat} = 0.2M_{\rm total,host}$ for the '$z = 0$' and '$z = 1$' experiments. In particular, the mass ratio between DM and luminous matter in the satellites is set to be the same as in the host galaxy. This implies that the mass of the stellar components of our satellites is 20 per cent of $M_{\rm disc,host}$, similar to those adopted in previous works on disc heating by satellite accretion (QHF93; WMH96; HC97; VW99). Note however that the initial total mass of the satellite is comparable to that of the host disc. For completeness, we also include the case of a satellite with a stellar mass of 10 per cent of $M_{\rm disc,host}$. In this case the total mass of the satellite is also 10 per cent of that of the host galaxy.

[1] Note that $\mathrm{sech}^2(\mathcal{Z}/2\mathcal{Z}_0) \approx \exp(-|\mathcal{Z}|/\mathcal{Z}_0)$ for $|\mathcal{Z}| \gg \mathcal{Z}_0$.

Table 2. Properties of satellite galaxies.

	'$z = 0$'	'$z = 1$'	
NFW halo			
Virial mass, $M_{\rm vir}$	2×10^{11}	1.01×10^{11}	($M_\odot$)
Virial radius, $R_{\rm vir}$	151.40	71.35	(kpc)
Concentration, c	16.18	8.09	
Circular velocity, $V_{\rm c}(R_{\rm vir})$	75.50	78.10	(km s^{-1})
$N_{\rm H}$	100 000	100 000	
Softening, $\epsilon_{\rm halo}$	0.14	0.07/0.14[a]	(kpc)
Disc			
Disc mass, $M_{\rm disc}$	5.6×10^9	2.4×10^9	($M_\odot$)
Scalelength, $R_{\rm D}$	1.69	0.96	(kpc)
Scaleheight, $\mathcal{Z}_0$	0.17	0.095	(kpc)
Toomre $Q(R = 2.4R_{\rm D})$	2.0	2.0	
$N_{\rm D}$	100 000	100 000	
Softening, $\epsilon_{\rm disc}$	0.024	0.007	(kpc)
Bulge			
Bulge mass, $M_{\rm bulge}$	5.6×10^9	2.4×10^9	($M_\odot$)
Scale radius, $a_{\rm b}$	0.9	0.709	(kpc)
Velocity dispersion, σ_0	96.29	69.06	(km s^{-1})
N_B	100 000	100 000	
Softening, $\epsilon_{\rm bulge}$	0.07	0.07	(kpc)

[a] Softenings used in discy and spherical satellites, respectively.

The spherical satellites lie on the observed fundamental plane of dE+dSphs galaxies (de Rijcke et al. 2005):

$$\log L_B \sim 4.39 + 2.55 \log \sigma_0, \quad (3)$$

$$\log L_B \sim 8.65 + 3.55 \log R_{\rm e}, \quad (4)$$

where L_B is the blue-band luminosity, and σ_0 is the central velocity dispersion. The effective radius is related to the scale radius by $R_{\rm e} \approx 1.82a_{\rm b}$ for a Hernquist density profile. Finally, we fix the mass-to-light ratio $\Upsilon_B = 2\Upsilon_{B_\odot}$ to derive the stellar mass of our spherical satellites.

The structural parameters of the discy satellites, $R_{\rm D}$ and $\mathcal{Z}_0$ are set in the same way as for the host.

The above relations fully specify the properties of our satellites, both for the '$z = 0$' and '$z = 1$' experiments. Note that the variation with redshift is always linked to that of the host halo. Table 2 lists the properties of both spherical and discy satellites for '$z = 0$' and '$z = 1$'.

2.3 Orbital parameters

We release our satellites from significantly larger distances than previous works (e.g. QG86; VW99; Kazantzidis et al. 2007). For the '$z = 0$' case, the satellite is launched from the virial radius of the host galaxy computed at $z = 1$ ($R_{\rm vir} = 122.22$ kpc $\approx 35R_{\rm D}$). For the '$z = 1$' experiment, it is launched from a distance of 83.9 kpc ($\approx 50\,R_{\rm D}$) which corresponds to the virial radius of the host galaxy computed at $z = 1.6$.

To initialize the orbital velocities of the satellites, we follow Benson (2005). Benson determined the orbital parameters of DM substructures at the time they crossed the virial radius of their host haloes (see also Tormen 1997; Khochfar & Burkert 2006). We choose for the velocities of our satellites the most probable values of the distributions as given for $z = 0$ (since little variation is visible as a function of redshift). The radial and tangential velocity distributions peak, respectively, at 0.9 and 0.6 in units of $V_{\rm c}(R_{\rm vir})$.

Table 3. Initial orbital parameters of satellite galaxies.

i	$\mathcal{X}$	$\mathcal{Z}$	$v_{\mathcal{X}}$	$v_{\mathcal{Z}}$	$L_{\mathcal{Z}}$
'$z = 0$'					
0°	122.2	0.0	−137.7	0.0	11219.8
30°	105.8	61.1	−119.2	−68.8	9716.6
60°	61.1	105.8	−68.8	−119.2	5609.9
'$z = 1$'					
0°	83.9	0.0	−118.2	0.0	6615.9
30°	72.7	42.0	−102.4	−59.1	5729.5
60°	42.0	72.7	−59.1	−102.4	3307.9

Notes. – Distances in kpc, velocities in $\mathrm{km\,s^{-1}}$, angular momentum in kpc km $\mathrm{s^{-1}}$.
– In all cases, $\mathcal{Y} = 0$ kpc, and $v_{\mathcal{Y}} = 91.8\,\mathrm{km\,s^{-1}}$ for '$z = 0$' and $v_{\mathcal{Y}} = 78.8\,\mathrm{km\,s^{-1}}$ for '$z = 1$'.
– Listed $v_{\mathcal{Y}}$ and $L_{\mathcal{Z}}$ are for prograde orbits. Retrograde orbits have the opposite sign.
– Initially $r_{\rm apo} = 77$ and 49 kpc, $r_{\rm peri} \sim 10$ and 5 kpc, respectively, for the '$z = 0$' and '$z = 1$' configurations (as measured from the first apocentre and the subsequent pericentre). The corresponding eccentricities $e = (r_{\rm apo} - r_{\rm peri})/(r_{\rm apo} + r_{\rm peri})$ are 0.77 and 0.82.

We consider for our satellites initial orbital inclinations of 0°, 30° and 60° (with respect to the plane of the host disc), in both prograde and retrograde directions with respect the rotation of the host disc. In the case of discy satellites, their mid-planes are parallel to that of the primary disc, implying that they are, respectively, inclined by 0°, 60° and 30° with respect to their orbital planes. Table 3 summarizes the orbital parameters adopted for both spherical and discy satellites, for the configurations at '$z = 0$' and '$z = 1$'.

Note that within each configuration, all the satellites are initially released from the same distance with the same velocity modulus, i.e. they all have the same total energy and modulus of the angular momentum, but the latter varying its orientation. This implies that the initial apocentre, pericentre (and hence orbital eccentricity) are the same for all experiments. However, as we shall see in Section 3.1 the orbits evolve due to dynamical friction, with some dependence on the internal properties of the satellite. Therefore, at the time the satellite merges with the disc, the orbits of all our experiments are different.

With these initial conditions, we find that our satellites have completely merged with the host discs by $z \approx 0.4$ and by $z \approx 1$, respectively, for the '$z = 0$' and '$z = 1$' cases.

2.4 Numerical parameters

The *N*-body systems are evolved using GADGET-2.0 (Springel 2005) a well documented massively parallel TREESPH code. Our choices of the numerical parameters (number of particles N in each component in the system; softening ϵ and time-step Δt) are described in detail in Appendix A.2. Tables 1 and 2 list the values used for each component in our simulations. The maximum time-step (not listed in the tables) is 0.25 Myr. Typically the energy and angular momentum are conserved to better than 0.1 per cent over 9 Gyr of evolution for our main disc galaxy configured at '$z = 0$'.

2.5 Evolution of isolated host galaxy

Before including the satellite, the host galaxy is simulated in isolation to test its stability in the absence of any external perturbation. As we show in Appendix A.3 our host galaxies are very stable in their properties (cf. VW99; Gauthier, Dubinski & Widrow 2006) for the amount of time needed to complete the experiments. Therefore, we are now ready to focus on how these systems evolve when they suffer a minor merger.

3 RESULTS

In total, 25 simulations have been carried out to study the formation and global properties of thick discs as a result of the merger between a host disc galaxy and a satellite. The simulations explore combinations of the following elements: two configurations for the progenitors ('$z = 0$' and '$z = 1$'); two morphologies for the stellar component of the satellite (spherical and discy); two total mass ratios between the satellite and the host galaxy (10 and 20 per cent) and three initial orbital inclinations for the satellite with respect to the mid-plane of the host disc (0°, 30° and 60°), in both prograde and retrograde directions.

3.1 Orbital evolution of the satellites

To study the evolution of the orbits in our experiments we follow the location of the centre of mass of the satellite (CM) with respect to the host galaxy. The CM is defined as the mean position of bound stellar and DM particles of the satellite. Fig. 1 shows the trajectories of the CMs for the experiments configured at '$z = 0$' and '$z = 1$' with a spherical satellite on a prograde orbit with initial inclination $i = 30°$. The $\mathcal{XY}$ projections clearly illustrate how radial the orbits are and how rapidly they decrease in amplitude due to dynamical friction between the satellite and the host system. Note that these orbits are quite different from the circular ones usually used in earlier studies (e.g. QG86; QHF93; WMH96). The $\mathcal{XY}$ and $\mathcal{XZ}$ projections show that the satellites stay on their original orbital planes as they decay, until they enter into the zone dominated by the host disc, when they are drawn on to the disc plane and spiral in towards its centre. This is particularly clear for the lighter satellite in our '$z = 1$' experiment that spends ∼1 Gyr on the disc plane before sinking in further.

Note that most of the angular momentum of the 'satellite+host system' is in the orbital motion of the satellites. This is because the satellites are relatively massive and have a very large initial distance from the host. As a result, when the satellite decays in an inclined

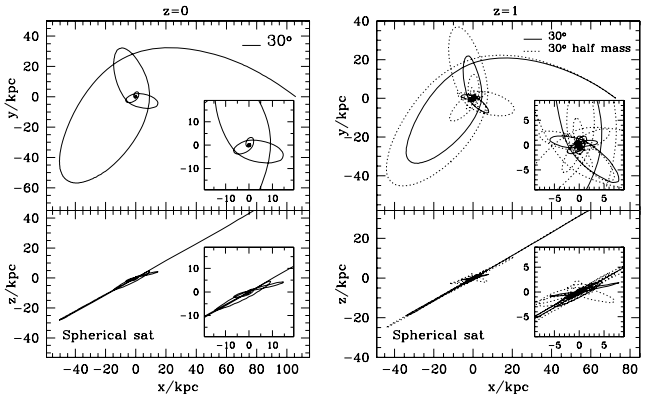

Figure 1. $\mathcal{XY}$ and $\mathcal{XZ}$ projections of the trajectory of the centre of mass of a spherical satellite as it decays towards the centre of the host galaxy in our '$z = 0$' and '$z = 1$' experiments with initial inclination 30°. The coordinate system is centred on the centre of mass of the host disc. The inset panels show in more detail the trajectory of the satellite at late times before it is fully disrupted.

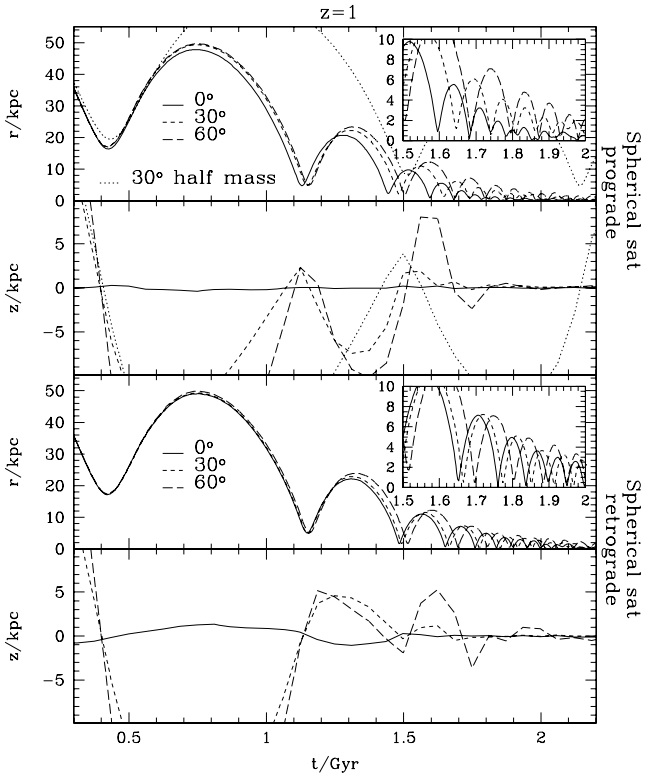

Figure 2. Evolution of the radial separation between the centres of mass of the host disc and the satellite, and of the $\mathcal{Z}$-distance of the satellite's centre of mass with respect to the host disc plane, for spherical satellites on prograde (top panels) and retrograde (bottom panels) encounters. The various curves correspond to different orbital inclinations for the '$z = 1$' configuration, and the 10 per cent experiment is shown for the inclination of 30°. The insets show in more detail the trajectory of the satellites at late times. The lack of a clear trend in the amplitude of the vertical oscillations is likely due to the difficulty in determining the exact orientation of the disc plane at the ∼1 kpc level. Similar behaviours are observable for the '$z = 0$' case.

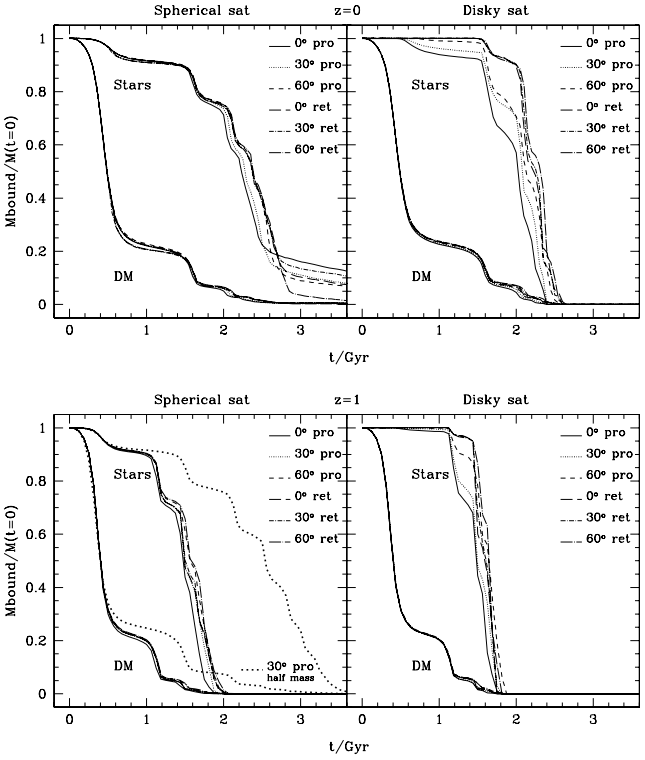

Figure 3. Mass that remains bound for both the DM and stellar components of the satellites in our experiments at '$z = 0$' (upper panels) and at '$z = 1$' (bottom panels). The bound mass is in units of the initial mass of the corresponding component.

orbit the disc is strongly tilted in both the prograde and retrograde cases (see Section 3.3).

As expected, the trajectory of the lighter satellite is more extended because dynamical friction is less efficient in this case (Binney & Tremaine 1987). Our 20 per cent satellites decay completely after ∼3 Gyr in the case of '$z = 0$' experiments, and after ∼2 Gyr for '$z = 1$' experiments. In comparison, the satellite with half of the mass takes the double of time to sink starting from the same initial orbital parameters. Initially, the orbital decay is due to the dynamical friction against the host halo. This implies that the decay rate does not depend on inclination, orbital direction or stellar mass distribution (see Fig. 2). On the other hand, when the satellites approach the centre of the system (where the disc is a significant contributor to the global force field), the orbit decays by dynamical friction also against the host disc. Thus at later times, prograde low-inclination orbits decay faster than retrograde or high-inclination orbits (QG86; WMH96; see also HC97).

3.2 Satellite mass loss

Fig. 3 shows the mass loss evolution of both DM and stellar components of spherical and discy satellites in the '$z = 0$' and '$z = 1$' experiments.

In order to calculate how much mass remains bound to the satellite at a given time we implemented in GADGET-2.0 the following procedure (Benson et al. 2004).

(i) Start by considering all the satellite particles that were bound to the satellite at the previous time-step (or simply all satellite particles for the first time-step).

(ii) Compute the mass of the satellite from these particles along with the position and velocity of the CM.

(iii) For each particle in this set, determine whether it is gravitationally bound to the other particles in the set.

(iv) Retain only those particles that are bound and go back to step (ii). Repeat until the mass of the satellite has converged.

Since the satellites were initialized in the absence of an external potential, as soon as they are placed within the host potential a large fraction (70 per cent) of the more extended DM component rapidly becomes unbound before the first pericentric passage. After that, the mass loss rate of the DM component mostly depends on its initial mass.

The mass loss rate of the stellar components depends strongly not only on initial mass, and orbital parameters (WMH96; HC97; VW99) but also on the stellar mass distribution. As satellites decay, prograde orbits with lower inclinations lose mass faster than retrograde orbits with higher inclinations, due to the stronger tidal interaction with the host galaxy. This trend is more notorious for discy satellites. Spherical satellites are also characterized by a more extended 'knee' in the mass loss in comparison to discy satellites. The lighter satellite experiences a slower mass loss compared to heavier satellites, because it suffers less dynamical friction and hence is on a less bound orbit.

Once a satellite has sunk onto the plane of the host disc, its fate will depend on its instantaneous mean density compared to the mean density of the host at a given location. If the mean density of the satellite is larger than that of the host system then the most bound particles of the satellite will reach the galactic centre as a distinctive core causing more damage to the host disc. Otherwise, the satellite will receive most of the damage, being heated and torn apart by the host disc. In our simulations only the mergers with spherical satellites in the '$z = 0$' experiments deposit in the galactic centre final cores of up to 20 per cent the initial stellar mass. These final cores are on the lighter side in comparison with previous studies using high-density satellites (QHF93, 20 per cent; WMH96, 45 per cent). It is interesting to note that spherical satellites with higher inclinations give rise to the formation of less massive cores. This can be explained by the fact that satellites on higher inclinations experience more disc crossings through the host disc as they decay, compared to ones on lower inclinations. In this case disc shocks perturb the structure of the satellite and cause additional mass loss (see Binney & Tremaine 1987; QHF93).

Fig. 3 shows that in general most of the DM is stripped off early, and deposited at very large radii (see Fig. 2). Therefore, the fraction of DM accreted from the satellite and deposited in a disc-like structure is very small in our simulations, in comparison to what Read et al. (2008) find. This may be explained by the fact that our satellites, although of comparable mass, are launched from much larger distances.

3.3 Description of the mergers

Fig. 4 illustrates the morphological changes in the host disc during merger events configured at '$z = 1$'. The initial inclination of the satellite is 30° for both prograde and retrograde orbits.

As the satellite decays in its orbit, it induces the formation of noticeable spiral arms in the host disc, which transport angular momentum from the central parts towards the outskirts. Once the satellite sinks on to the plane of the host disc it transfers kinetic energy from its orbit to the particles in the disc, increasing their vertical motions and causing a visible thickening. At the same time the disc responds to the decaying satellite, by tilting its plane in order to conserve the total angular momentum of the system (although a significant amount of the satellite's initial angular momentum has by this time, already been transferred to the host halo).

Figs 5 and 6 show the distribution of stellar particles for both spherical and discy satellites on prograde orbits with initial inclination 30°. In the early stages of the orbital decay, the satellite is stripped leaving trails of particles on orbits with inclinations similar to that of the satellite initially. Since the stars are initially deeply embedded in the satellite's DM halo, only a small fraction of the stellar debris is deposited at large radii. Most of the stars from the satellite end up in a disc-like configuration, with the same orientation as the final disc, but one that is somewhat thicker and more extended (see Section 3.4). Noticeable shells of debris material are formed as time goes by. These structures are a consequence of the interaction

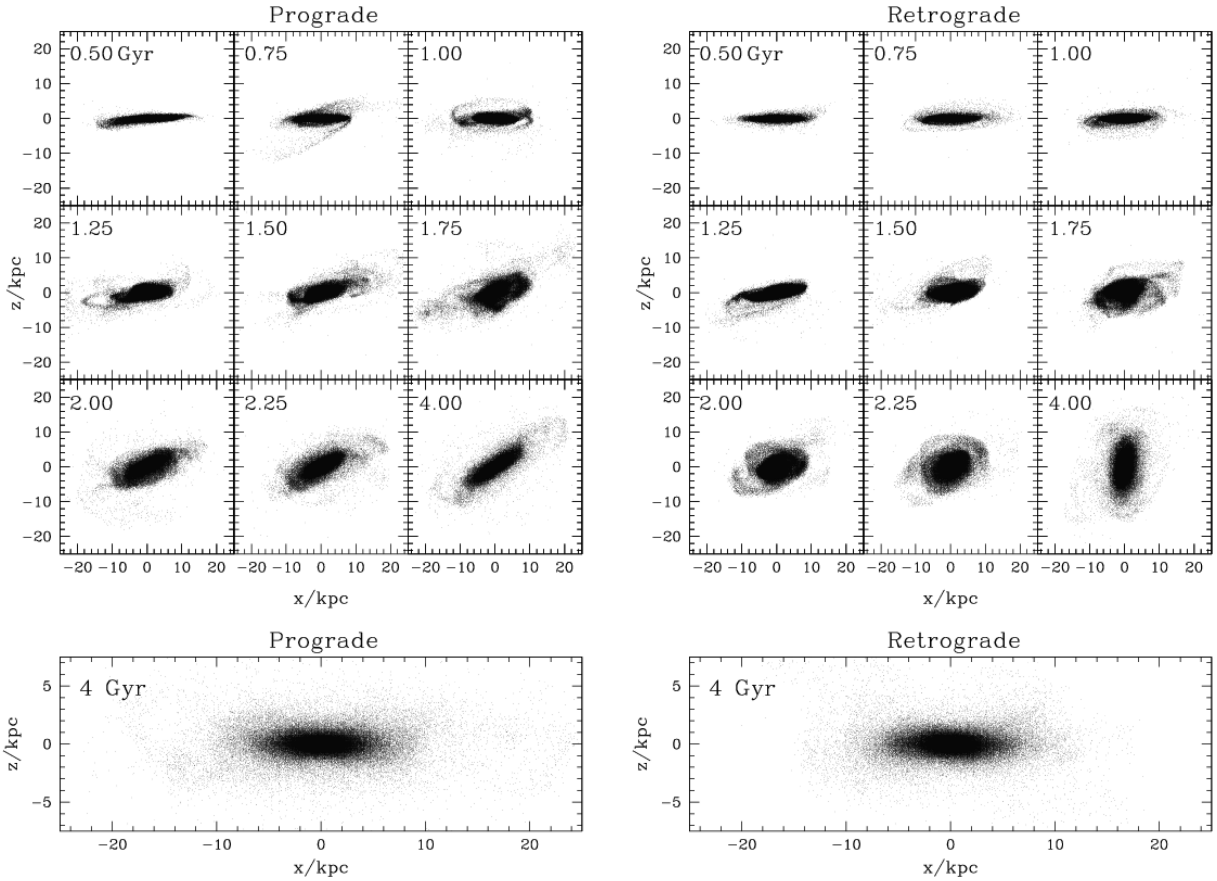

Figure 4. Evolution of the host disc (initially shown edge-on) during the merger with a spherical satellite with inclination of 30° for prograde and retrograde orbits in the '$z = 1$' experiment. Only host disc particles are shown for clarity. Note that the disc appears over thickened or distorted because of projection effects, especially in the case of the retrograde orbit. The bottom panels show edge-on views of the final system.

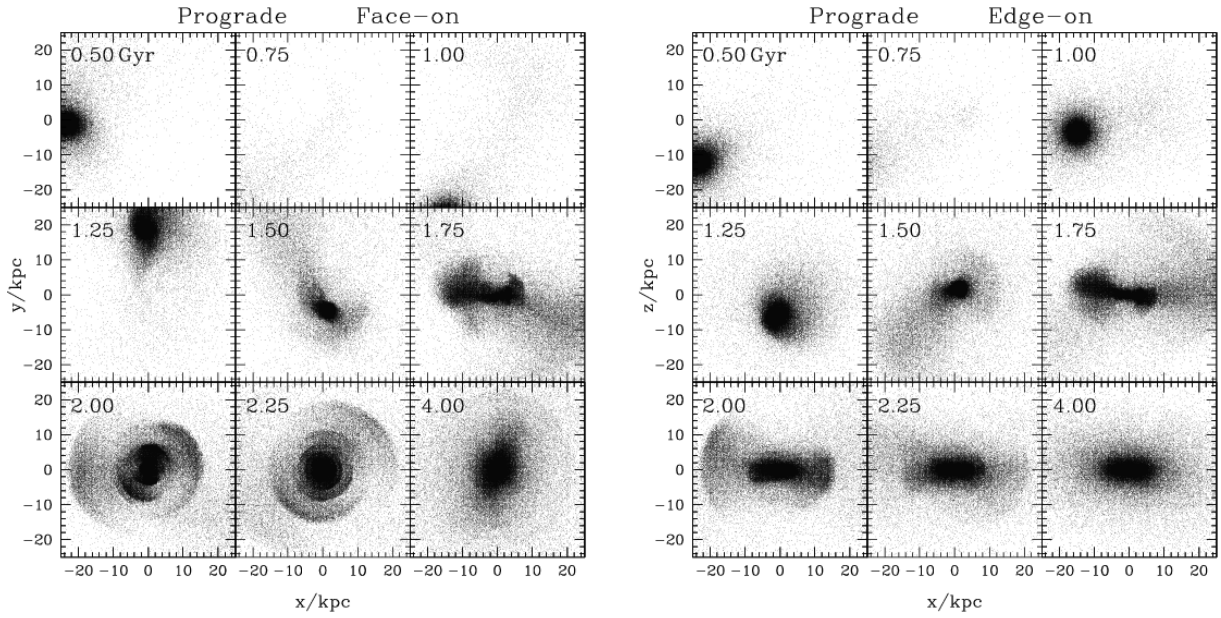

Figure 5. Evolution of the spherical satellite with inclination 30° during the prograde merger with the host galaxy in the '$z = 1$' experiment. In each snapshot the reference frame has been centred on the centre of mass of the host disc and has also been rotated to eliminate the tilting of the whole system with respect to the original frame. The labels *face-on* and *edge-on* are relative to the host disc (not shown here for clarity).

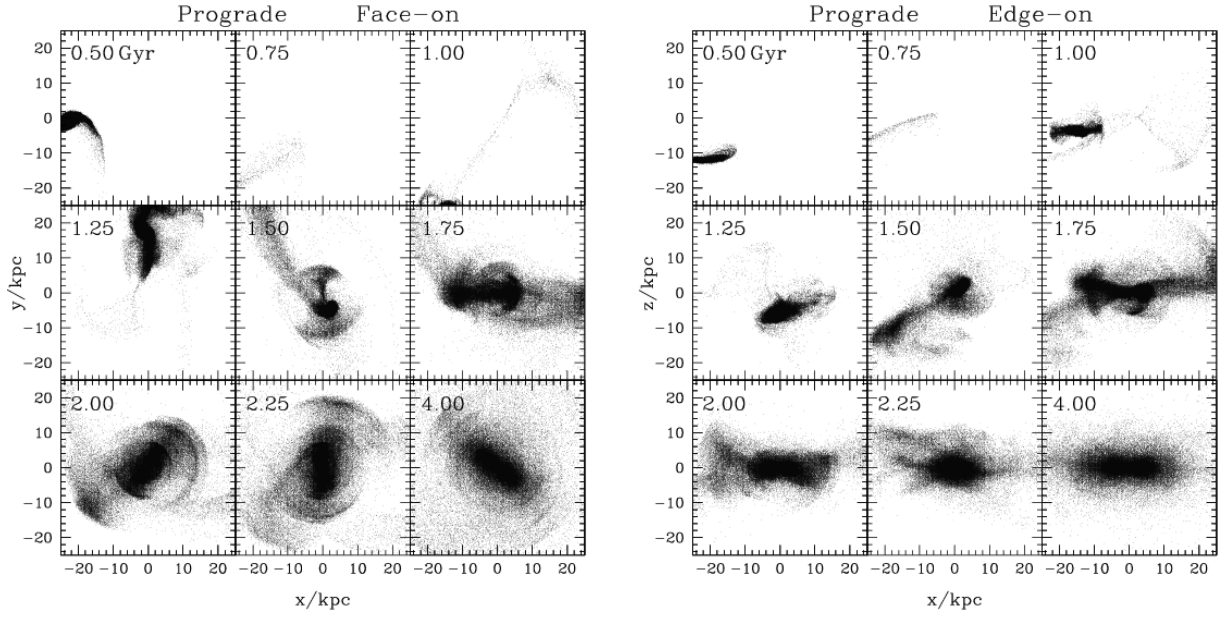

Figure 6. Same as Fig. 5, but for the case of the discy satellite.

of a dynamically cold system with a larger one (Hernquist & Quinn 1988). In general the survival of these shells will depend on the mean phase-space density of the infalling satellite and also on its orbit. In the case of spherical satellites shells are visible typically since $t \sim 1.7$ Gyr, lasting $\sim$2 Gyr; and for discy satellites much sharper shells are seen starting at $t \sim 1.5$ Gyr, being still noticeable by the end of the simulation, i.e. $\sim$2.5 Gyr later. Shells are rather common features related to merger events, being observed in many elliptical and spiral galaxies. An important characteristic of shells is that they usually survive for a long time in physical space, as previous numerical studies have shown (e.g. Hernquist & Quinn 1988, 1989). The presence of such a structures in the solar vicinity and the possible signatures imprinted on them during the formation of the thick disc will be explored in Paper II (note that such features have already been proposed to explain the Monoceros ring, see e.g. Helmi et al. 2003).

3.4 Properties of the merger products

By the end of the simulations the morphological, structural and kinematical properties of the heated discs and satellite debris have settled down and do not evolve further. This occurs $\sim$2 Gyr after either the satellite has been disrupted or its core has reached the centre of the host disc. This means that the properties of the final

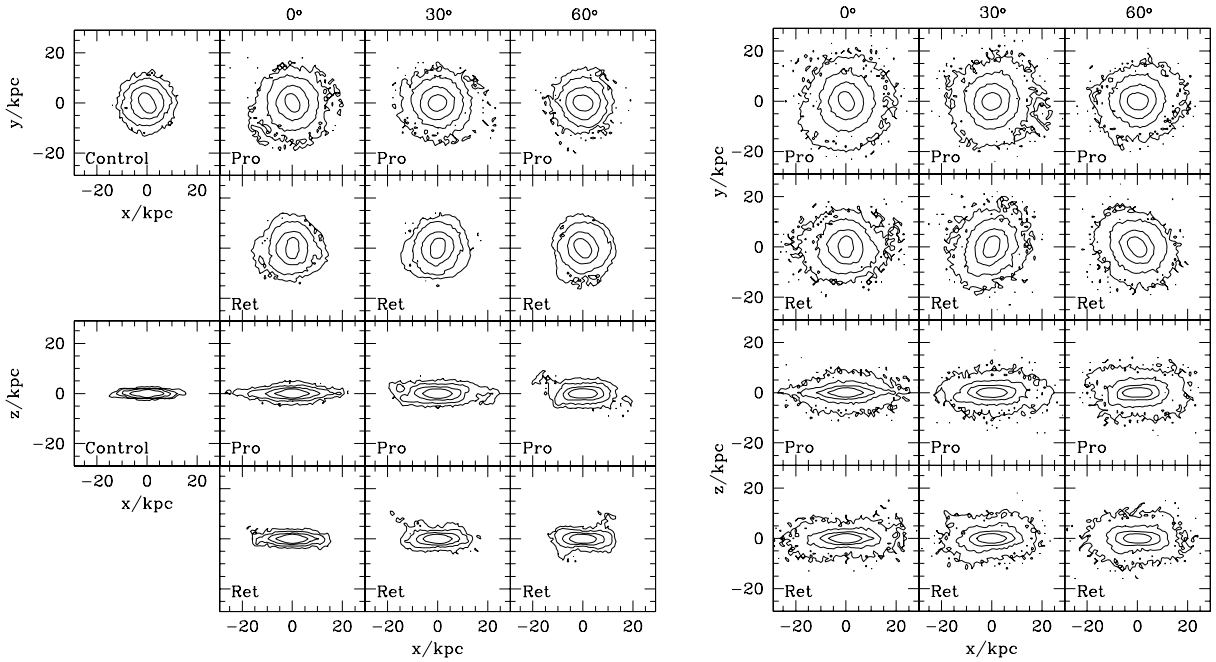

Figure 7. Face-on and edge-on views of the final morphologies of heated discs (left) and thick discs (right) at the end of the simulations in '$z = 1$' experiments, 4 Gyr after the infall of the spherical satellite. In each case the tilting induced by the satellites has been eliminated to facilitate the comparison with the coeval control disc. The contours correspond to 4.5, 6.2, 8 and 9.7 mag below the central surface brightness of the remnant system. For the experiments shown here, and assuming a mass-to-light ratio $\Upsilon_V = 2\Upsilon_{\odot,V}$, these would be located at 22.5 (innermost), 24.2, 26 and 27.7 mag arcsec^{-2} (outermost) in the V band.

thick discs do not change after $t = 5$ and 4 Gyr for the systems configured at '$z = 0$' and at '$z = 1$', respectively, in the case of heavy satellites. This time-scale is ∼6 Gyr for the lighter satellite in our '$z = 1$' experiment.

We now study in more detail the characteristics of the final discs. To this end we use a reference frame centred on the centre of mass of the final product, and aligned with its principal axes in such a way that the rotation axis defines the $\mathcal{Z}$-direction.

3.4.1 Morphological properties

The left-hand panels in Fig. 7 show the morphologies of the heated host discs at the final time of the '$z = 1$' experiments ($t = 4$ Gyr), for the case of the spherical satellites. Prograde orbits and lower inclinations induce on the host moderate arms and more radial expansion in comparison with retrograde orbits and higher inclinations. On the other hand, higher prograde inclinations are more efficient at thickening the disc, especially in the outskirts. For instance, a prograde satellite with inclination of 60° only causes a slight increment of the radial extension compared to the coeval control disc, but induces a noticeable thickening compared to the same control disc and to the other inclinations. Satellites on retrograde orbits have a similar thickening effect on the disc but a considerably milder influence on the formation of tidal arms and radial expansion compared to satellites on low inclination prograde orbits. Notice also that the satellites during their decay can induce the formation of weak bars (see also Berentzen et al. 2004). Some warping in the discs is also visible in the case of mergers with inclinations of 60° for both prograde and retrograde orbits (see also QHF93; VW99).

The panels on the right-hand side of Fig. 7 show the thick discs obtained, now including the contribution of the satellite's stellar particles. Their final structure is dominated by the heated disc (compare to the left-hand panels), except in the outer regions, where the contribution of satellite debris is important. The outskirts are clearly thicker for satellites on higher inclination orbits, although their debris does not show the warp feature characteristic of the heated discs. Also noticeable is the difference in the distribution of satellite debris between prograde and retrograde orbits for the case of coplanar infall (in edge-on views).

The contour levels shown in this figure have been drawn 4.5, 6.2, 8 and 9.7 mag below the central surface brightness of the remnant system. If we assume a mass-to-light ratio $\Upsilon_V = 2\Upsilon_{\odot,V}$ for the host as well as for the satellite stars, these contours correspond to 22.5, 24.2, 26 and 27.7 mag arcsec^{-2} in the V band, respectively.

It is useful to compare this to the sample of late-type edge-on galaxies observed by Dalcanton & Bernstein (2000) (their fig. 3) and DB02 (their fig. 1), who typically probe up to ∼5 mag below the central surface brightness of their (thin + thick) discs in the R band. Their faintest contour would be located in between the first and second brightest contours shown in the right-hand panels of Fig. 7. At least qualitatively, the surface brightness distribution of the remnants in our simulations resembles those observed by these authors.

We further quantify the shapes of the isophotal contours of the remnants by obtaining their photometry with the task ELLIPSE (Jedrzejewski 1987) of the data reduction package IRAF.[2] This task draws an ellipse to approximately match an isophote and then expands the intensity along the ellipse as a Fourier series. According to Bender, Doebereiner & Moellenhoff (1988), the most significant non-zero component of this Fourier analysis is the a_4 parameter

[2] IRAF is distributed by the National Optical Astronomy Observatories, which are operated by the Association of Universities for Research in Astronomy, Inc., under cooperative agreement with the National Science Foundation.

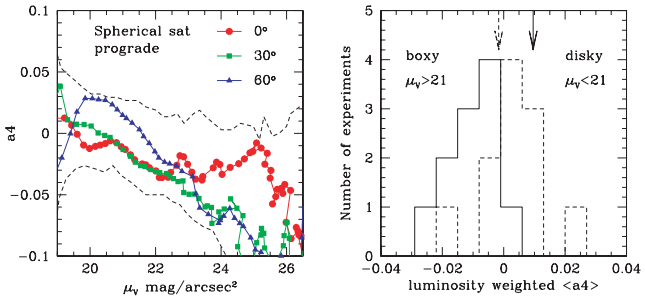

Figure 8. Left: a_4 versus surface brightness in the V band for our '$z = 1$' experiments of a spherical satellite on a prograde orbit. The dashed curves delimit the region where all experiments fall. Note that the central surface brightness of our remnant discs are $\mu_{V,0} \sim 18$–$19\,\mathrm{mag\,arcsec^{-2}}$. Right: luminosity weighted distribution of the a_4 parameter for all our '$z = 1$' experiments. The dashed histogram corresponds to the a_4 obtained by considering the region enclosed within an isophote with $\mu < \mu_0 + 3$, while the solid one to $\mu_0 + 8 > \mu > \mu_0 + 3$. The arrows show the values of $\langle a_4 \rangle$ for the coeval control simulation.

[corresponding to the cos (4θ) term]. Isophotes are then characterized as either discy ($a_4 > 0$) or boxy ($a_4 < 0$).

To mimic the observations, we have created artificial images out of the simulated thick discs from an edge-on point of view, by binning a central area ($\sim 15 \times 15$ scalelengths of the initial primary disc) into 1024×1024 pixel. When running ELLIPSE on these images, we have allowed the geometric centre, ellipticity and position angle of the isophotes to vary freely, taking linear steps of 5 pixel along the semimajor axis. We have also made sure that our results are robust to the initial guesses for the values of the various parameters required by ELLIPSE.

The left-hand panel of Fig. 8 shows the a_4 parameter as a function of isophotal surface brightness in the V band for our '$z = 1$' experiments. To avoid cluttering only experiments with spherical satellites on prograde orbits are explicitly shown. The rest fall in the region delimited by the dashed envelopes. This figure shows that the isophotes go from more discy at higher surface brightness (i.e. in the central regions) to more boxy at lower surface brightness, presenting a mild trend with initial inclination of the satellite.

DB02 performed a similar analysis on their sample (see their fig. 11). They find that inner isophotes with a surface brightness level of $\sim$3 mag below the typical peak level for their sample ($21\,\mathrm{mag\,arcsec^{-2}}$) are discy, while outer isophotes (defined as those $\sim$5 mag below the peak) are as likely to be boxy as discy.[3] Similarly to DB02, in the right-hand panel of Fig. 8 we plot the distribution of a_4 (weighted by both errors and luminosity) for both inner and outer regions including all the '$z = 1$' experiments. The inner region is defined to be within 3 mag from the peak surface brightness, as done by DB02. The outer region extends down to 8 mag below the central surface brightness value. This figure confirms that inner isophotes are discy while outer ones appear clearly boxy. This may suggest that deeper photometry, beyond the limit reached by DB02 would be needed to detect the predominantly boxy shape of the contours in the outskirts of our remnants.

The boxy nature of the outer isophotes, which is present in all our experiments, could in principle be used as a discriminant for the formation of thick discs via mergers such as those studied here.

[3] It is important to keep in mind that DB02 use a different procedure to quantify the isophotal shape, meaning that the values of their shape parameters are not directly comparable to ours.

However, it should be borne in mind that the degree of boxiness in the remnants also depends on the initial structure of the host system. For example, studies which have a spherical centrally concentrated core component (bulge or cored DM profile) produce a remnant which is less boxy (Naab & Burkert 2003; Bournaud et al. 2005). This is because such spherical components act in a stabilizing sense for the disc (VW99; Kazantzidis et al. 2007), which therefore retains more closely its original morphology. This would imply that boxy isophotes are not necessarily direct evidence in support of the scenario proposed in this paper, but that they should be more prominent in the thick discs present in bulgeless galaxies.

3.4.2 *Structural properties*

We now describe in detail the structural properties of the remnant systems produced in our experiments. We first address their vertical structure and show explicitly the need to include two components (thin and thick). We then use the information obtained from the vertical decomposition to characterize the radial extension of both disc components. Finally, the spatial distribution of stars from both the primary disc and the satellite are compared.

Note that, as mentioned above, before measuring the discs, these have been properly centred and aligned, so the rotation axis defines the $\mathcal{Z}$-direction. Furthermore, all the properties have been computed taking into account star particles from both the host disc and the satellite. Their relative contribution has been appropriately weighted according to the initial $M_{\mathrm{sat,stars}}/M_{\mathrm{host,disc}}$ ratio to account for the fact that the satellite particles have smaller masses.

3.4.2.1 Vertical structure of the remnants Fig. 9 shows the vertical luminosity distributions of the remnant systems for all our experiments. These have been obtained by including all stars at all radii within $|\mathcal{Z}| < 3\,\mathrm{kpc}$ for '$z = 1$', and within $|\mathcal{Z}| < 5\,\mathrm{kpc}$ for '$z = 0$'. The dotted lines correspond to a single-component sech^2 fit to the vertical profile. This figure shows that such a model clearly underestimates the luminosity at large distances from the plane, highlighting the need for a two-component decomposition.

Therefore, we fit the surface brightness as

$$L(R, \mathcal{Z}) = \sum_{i=1}^{2} L_{0,i}(R)\,\mathrm{sech}^2\left(\frac{\mathcal{Z}}{2\mathcal{Z}_{0,i}}\right), \qquad (5)$$

where $\mathcal{Z}_{0,i}$ is a (luminosity weighted) exponential scaleheight and $L_{0,i}$ is the central luminosity (on the mid-plane) of each component ($i = 1, 2$). As usual, $\mu(R, \mathcal{Z}) = 26.4$–$2.5\,\log[L(R, \mathcal{Z})]$. To compute the luminosity-weighted scaleheights we proceed as follows. First, we fit independently the vertical brightness profiles in 1 kpc radial bins (within projected radii $R < 20\,\mathrm{kpc}$ for '$z = 0$', and $R < 10\,\mathrm{kpc}$ for '$z = 1$') using two components. For each radial bin we allow the algorithm to find the best central luminosities and exponential scaleheights using a Levenberg–Marquardt least-squares minimization. The luminosity-weighted scaleheight of each component is then the mean scaleheight averaged over all radii and weighted by luminosity.

The fits obtained in this way are shown in Fig. 9 as solid curves. Clearly the vertical structure of our remnants is considerably better modelled by considering two disc components with different scaleheights and central surface brightness. In all cases, a thin disc is present after the merger with the satellite.

Fig. 10 shows the luminosity-weighted scaleheights of each component of the remnant systems for all our experiments. Note that the thinner component has in all cases, a very similar (and only slightly

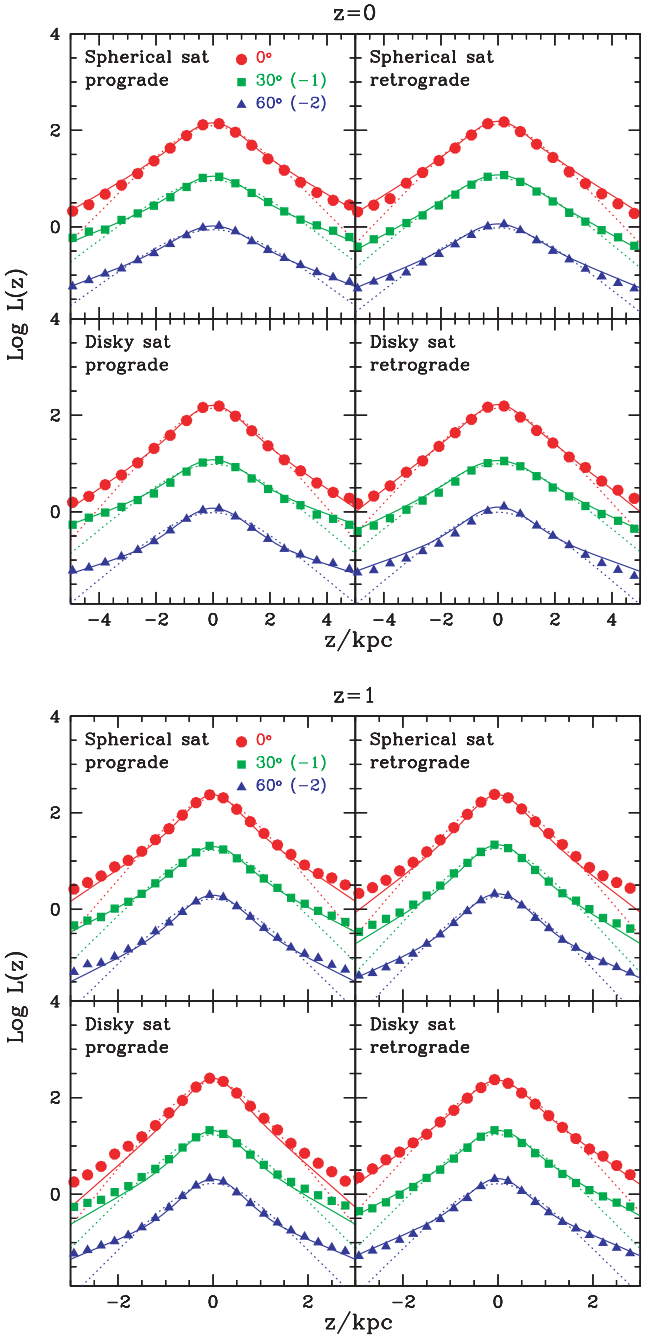

Figure 9. Vertical luminosity profiles (integrating over all radii at each height) for each of our experiments. Fits using only one component (dotted lines) systematically underestimate the luminosity far from the mid-plane. Two-component fits (solid lines) are clearly a better representation of the vertical structure of our remnant discs. Note that, for clarity, profiles of inclinations of 30° and 60° include offsets of log(L)– 1 and log(L)– 2, respectively.

larger) scaleheight to that of the initial host disc. The scaleheight of thicker component is clearly larger for encounters with higher orbital inclinations. This is because there is a significantly larger vertical kinetic energy associated to the satellites' orbital motion transferred to the disc. Spherical and discy satellites do not induce very different vertical heating on the discs. Note that less massive satellites produce final thick discs that are thinner.

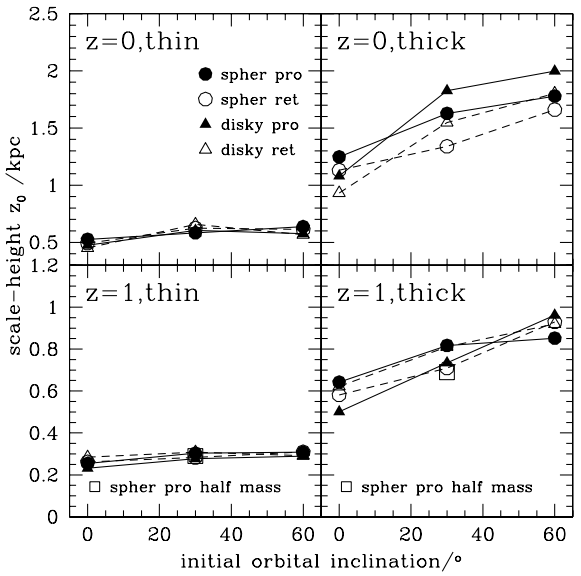

Figure 10. Scaleheights of the final systems decomposed into a 'thin' and a 'thick' disc. Solid/dashed lines connect prograde/retrograde satellites.

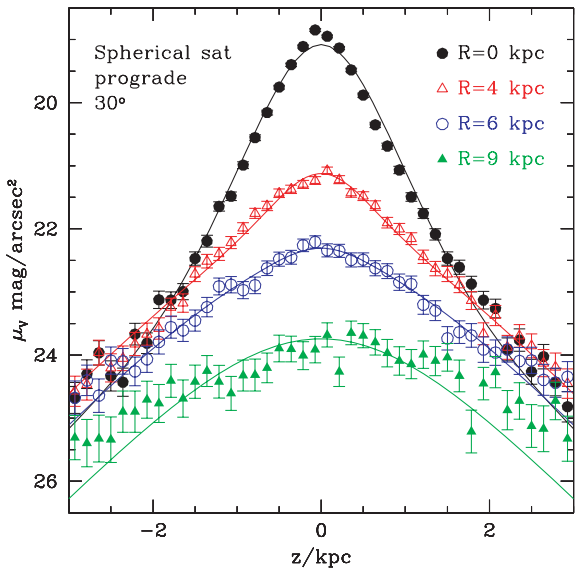

Figure 11. Surface brightness profiles as a function of height at several projected radii for one of the '$z = 1$' experiments. The thin remnant dominates the surface brightness in the central regions, while the thicker component is more dominant at the outskirts. Solid lines show the two-component fits at each radius.

Fig. 11 shows surface brightness profiles as a function of height at several projected radii for one of the experiments. Two-component fits using the luminosity-weighted scaleheights described above are also included. This figure shows that the remnant thin disc dominates the surface brightness at small radii. Note that at large radii ($R = 9$ kpc, or $\mu \sim \mu_0 + 6$) there is an indication that the thick disc is flared, and no longer follows an exponential distribution with a constant scaleheight at all radii. Such flared discs have already been observed in previous studies (e.g. QG86), suggesting that flaring is a rather generic characteristic of discs heated by mergers (see Kazantzidis et al. 2007, for a derivation of how the scaleheight varies with radius due to minor mergers).

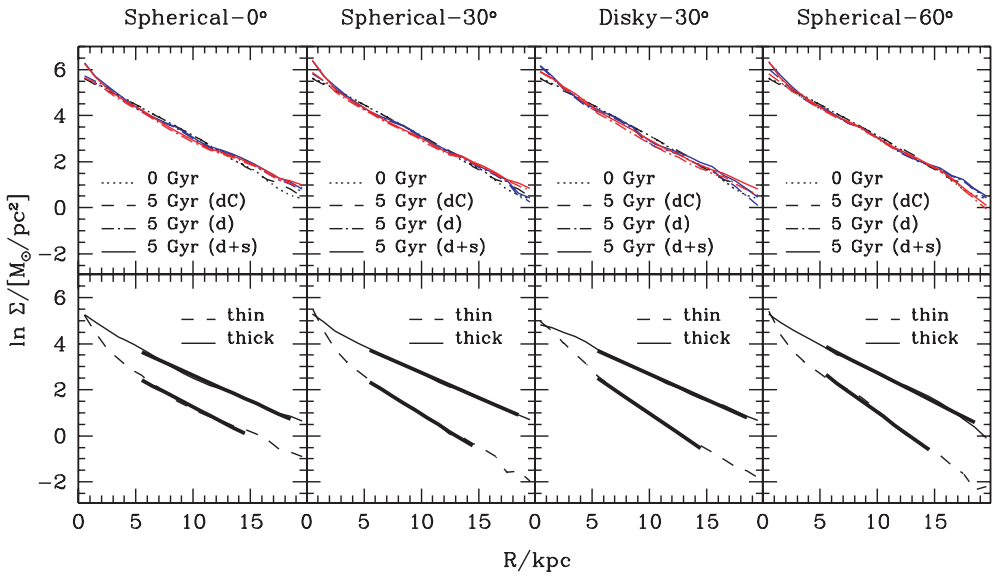

Figure 12. Upper panels: surface density profiles of final thick discs as a function of cylindrical radius for '$z = 0$', including stars within $|\mathcal{Z}| < 5$ kpc. Red and blue lines correspond to prograde and retrograde orbits, respectively. The measurements include stars of both disc and satellite (solid) or only stars from the disc (dashed–dot). As reference, both initial (dotted) and final states (dashed) of the disc in the control model are also shown. Lower panels: surface density profiles of regions dominated by thin (dashed; defined by $|\mathcal{Z}| < 0.5\ \mathcal{Z}_{0,\rm thin}$) and thick (solid; $1\ \mathcal{Z}_{0,\rm thin} < |\mathcal{Z}| < 5$ kpc) remnants, including the section used to compute the scalelengths (heavy solid).

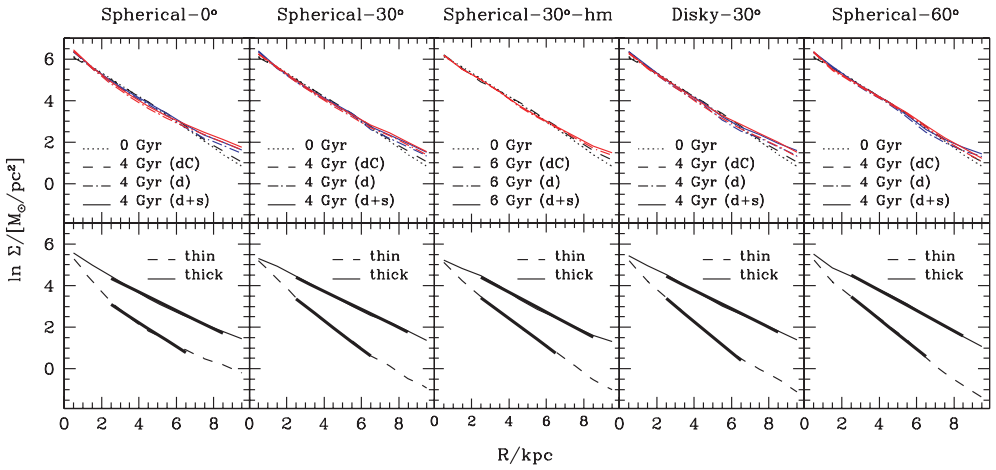

Figure 13. Same as Fig. 12 but now for the '$z = 1$' experiments, including stars within $|\mathcal{Z}| < 3$ kpc in the upper panels. In this case the region dominated by thick remnants is defined as $1\ \mathcal{Z}_{0,\rm thin} < |\mathcal{Z}| < 3$ kpc. The column 'hm' corresponds to the lighter satellite (with half the mass).

3.4.2.2 Radial structure of the remnants Figs 12 and 13 show the mass surface densities of the simulated thick discs as a function of radius, for the '$z = 0$' and '$z = 1$' configurations, respectively. Each panel is for a different inclination or different type of satellite (spherical, discy or half-mass) on prograde (red) and retrograde orbits (blue). The control disc galaxies are also shown at the initial (dotted curves) and final times (dashed curves) to calibrate the effect of the mergers against the intrinsic evolution of the host (which in all cases is negligible). In order to estimate the contribution of the satellite stars, the mass surface densities of only host discs are plotted separately (dash–dotted curves).

For both '$z = 0$' and '$z = 1$' experiments, the surface density profiles show a mild dependence on orbital inclination (upper panels), having slightly higher surface brightness in the outskirts for lower inclinations. This tendency is mostly due to the host disc material that is transported radially outwards during the merger by transfer of energy and angular momentum.

As expected, the lighter spherical satellite (in the '$z = 1$' experiment) produces a smaller variation in the surface density at larger radius. In general the contribution of satellite particles to the spatial structure of final thick discs is very small. This is true at all radii except at the centre where the very dense spherical satellites accreted in the '$z = 0$' experiment are not completely disrupted, retaining a core and giving rise to a small 'bulge-like' component (see also Fig. 3). The surface density profile does not show any strong dependence on orbit direction.

The lower panels of Figs 12 and 13 show the surface density profiles of regions dominated either by the thin or thick remnants (for prograde experiments only) according to the decomposition performed in Section 3.4.2.1. These regions are defined as

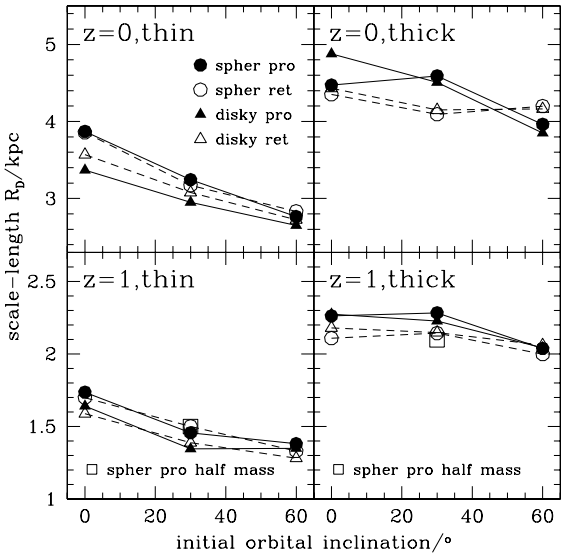

Figure 14. Scalelengths of the remnant system for all experiments. They are obtained by decomposing the final discs into thin and thick components. Solid/dashed lines connect prograde/retrograde satellites.

$|\mathcal{Z}| < 0.5\mathcal{Z}_{0,\rm thin}$ for the thinner component, and for the thicker one from 1 $\mathcal{Z}_{0,\rm thin}$ up to 5 kpc for the '$z = 0$' case (and up to 3 kpc for '$z = 1$'). The scalelengths of each component are computed by applying a linear fit to $\ln\Sigma(R)$, avoiding non-axisymmetries associated to both the central regions and the very outskirts. Note that the linear fits consider a more extended region for thick remnants. This is to account for the dominance of thick remnants at larger radii (see Fig. 11).

Fig. 14 shows the final scalelengths of the thick discs as a function of the initial orbital inclinations of the satellites. In all cases, the remnant thin discs have smaller scalelengths than their thicker counterparts, and comparable to the initial values. Low inclination encounters induce larger thick-disc scalelengths in comparison to higher inclinations. This is because in the former cases, the orbital energy of the satellite is deposited mostly into radial motions of the stars in the disc. Similar trends are observed for the galaxies in Yoachim & Dalcanton (2006). However, this should be taken with great care because our comparison is to the remnant thin disc and not to the present-day thin disc of those galaxies (because we do not model this). Furthermore, we have not modelled the response of the remnant thin or thick discs to the formation of the new thin disc.

We compute the total mass associated to each of disc component using the fits just derived. We find that the total mass associated to the remnant thin disc is ∼15–25 per cent of the total stellar mass of the system for both '$z = 0$' and '$z = 1$' experiments.

In general, the presence of a thin remnant after the merger is in agreement with results by Kazantzidis et al. (2007), although the total mass associated to this component is significantly smaller in our case (<25 versus ∼80 per cent). This is maybe due to the fact that Kazantzidis et al. (2007) do not follow the full merger event, but only let their satellites have one passage around their host disc, hence perhaps increasing its chances of remaining relatively cold. Note, however, that in their work this bombardment is repeated in a sequence using six different satellites.

3.4.2.3 Distribution of satellite versus host disc stars Fig. 15 shows the final relative number $N_{\rm s}/(N_{\rm s} + N_{\rm d})$ of stellar satellite particles as a function of radius in the resulting thick discs for mergers configured at '$z = 0$' and '$z = 1$'. Recall that the number of satellite particles has been renormalized according to $N_{\rm s} = N_{\rm sat,stars}\, M_{\rm sat,stars}/M_{\rm disc}$.

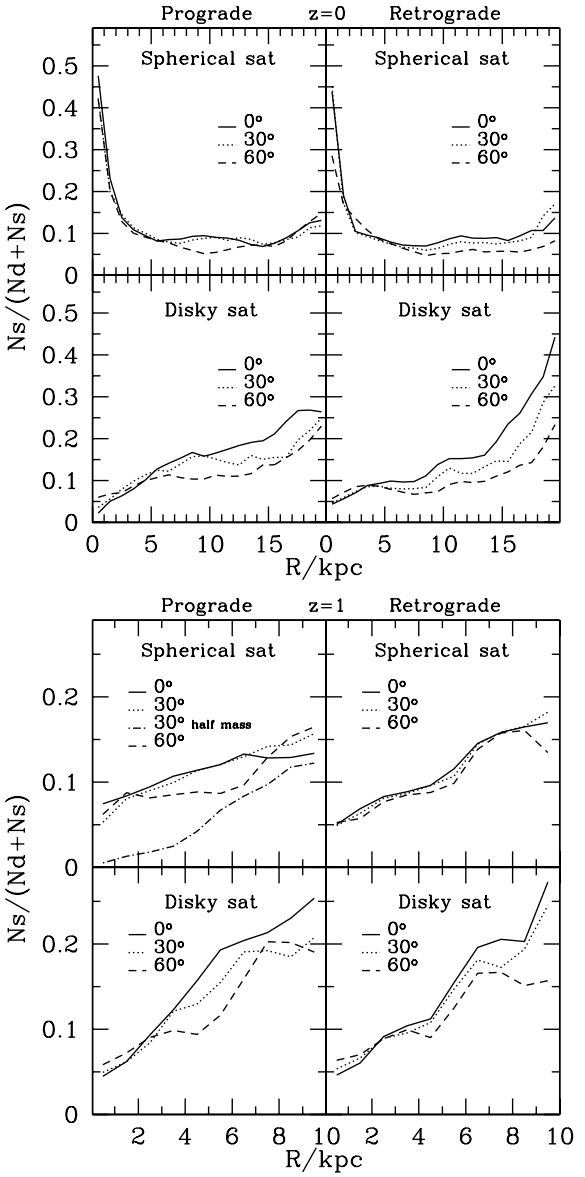

Figure 15. Relative number of satellite particles in the final systems as a function of cylindrical radius for the '$z = 0$' (top) and '$z = 1$' (bottom) experiments.

As mentioned before, in the '$z = 0$' experiments, spherical satellites have a higher mean density that the host disc. This causes the core to reach the host disc centre almost intact, representing ∼50 per cent of the total number of particles near the centre of the final thick disc. In comparison, this ratio drops to 5 per cent for the discy satellites. At both intermediate and larger radii the fraction of particles from the spherical satellites is roughly constant, independently of either orbital inclination or sense of rotation. On the other hand, discy satellites are disrupted at large radii, where their debris is deposited. Furthermore, the lower the inclination, the higher the fraction at a given radius, as naturally expected.

For '$z = 1$' both spherical and discy satellites are completely destroyed. The relative fraction of satellite stars increases with radius and, as expected, at the centre the relative number of satellite particles is smaller for the lighter satellite. The observed trend with orbital inclination in spherical and discy satellites at '$z = 0$' is confirmed for the '$z = 1$' configuration.

Fig. 16 shows the fraction of satellite particles plotted now as a function of the vertical direction at a radius $R = 4.5$ kpc, for spherical and discy satellites in the '$z = 1$' experiments. The radius corresponds to 2.4 initial scalelengths in this experiment. In this figure the distances from the plane are normalized by the scaleheight obtained by fitting locally a single sech^2 law to the vertical density distribution. Therefore, Z_0 is close to a luminosity weighted average of the scaleheights of the thin and thick discs given in Fig. 10. This figure shows that the fraction of accreted particles as a function of distance from the plane, when normalized by this scaleheight, *only* depends on the mass ratio between the satellite and host. E.g., at $\mathcal{Z} = 4Z_0$ the fraction of particles reflects the mass ratio of the merger. The same behaviour is observed in the '$z = 0$' experiments.

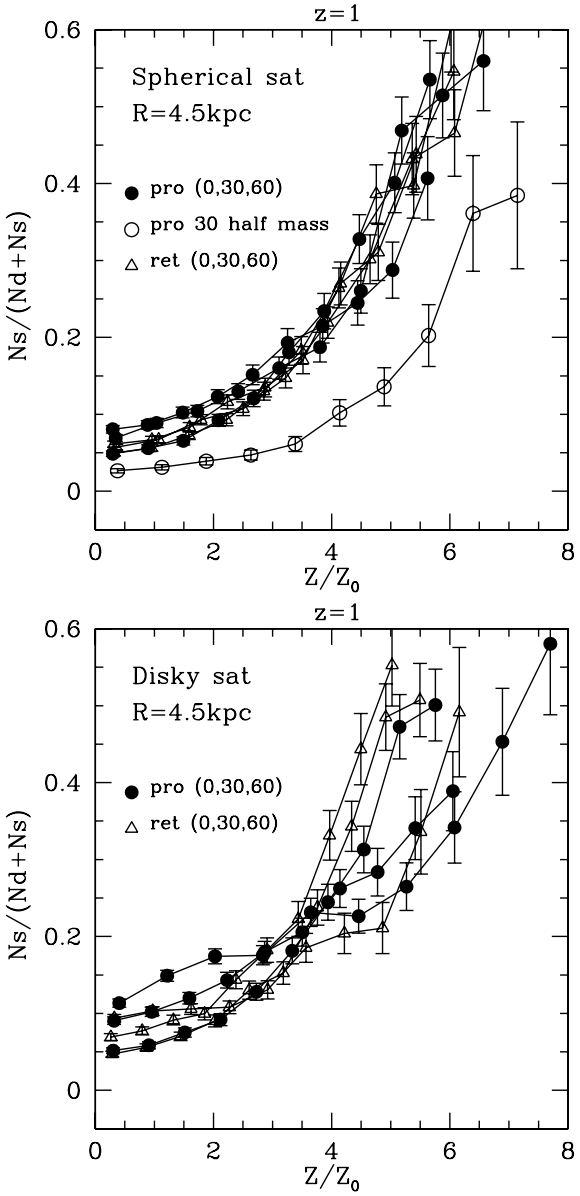

Figure 16. Relative number of satellite particles for our '$z = 1$' experiments, as a function of distance from the disc plane. Distances from the plane are normalized by the respective scaleheight at a distance of $R = 4.5$ kpc (i.e. 2.4 scalelengths of the original disc). Note that the scaleheight here is obtained by fitting locally a single sech^2 law to the vertical density distribution, and hence it is close to a luminosity weighted average of the scaleheights of the thin and thick disc shown in Fig. 10.

3.4.3 *Kinematical properties*

The structural decomposition made in Section 3.4.2.1 should also be reflected in the kinematics of the stars in our systems in order to be physically meaningful. Fig. 17 shows this is indeed the case. Here we plot the $\mathcal{Z}$ velocity distribution within a spherical volume of 1-kpc radius centred at $R \sim 4$ kpc on the mid-plane for one of our experiments ('$z = 1$', spherical satellite, prograde, 30°). The dashed curve shows that a single Gaussian (corresponding to a one-component system) misses the peak of the distribution highlighting the need for a second (colder) component. We therefore proceed to fit all velocity distributions (also the radial and azimuthal) with two Gaussians. We constrain the relative normalization of these by using the photometric decomposition from Section 3.4.2.1, which determines the relative number of stars from each component within a given volume. The solid curve in Fig. 17 is an example of the quality of the fit obtained in this way, whose reduced χ^2 (= 0.47) is lower than that obtained for a single Gaussian (= 0.68).

The transformation of orbital energy into thermal energy (random motions) in the disc is evident in Figs 18 and 19. Here we show the radial, azimuthal and vertical velocity dispersions along with the mean rotational velocities of the thick discs present in our systems as a function of cylindrical radius. These quantities have been computed at each cylindrical radius in concentric rings of 1 kpc width, including stars between $|\mathcal{Z}| < 3$ kpc for '$z = 0$', and $|\mathcal{Z}| < 1.5$ kpc for '$z = 1$' experiments.

In all our experiments, the vertical and azimuthal velocity dispersions of the remnant thin discs are very similar to those of the initial host disc, and hence are not plotted for clarity. On the other hand,

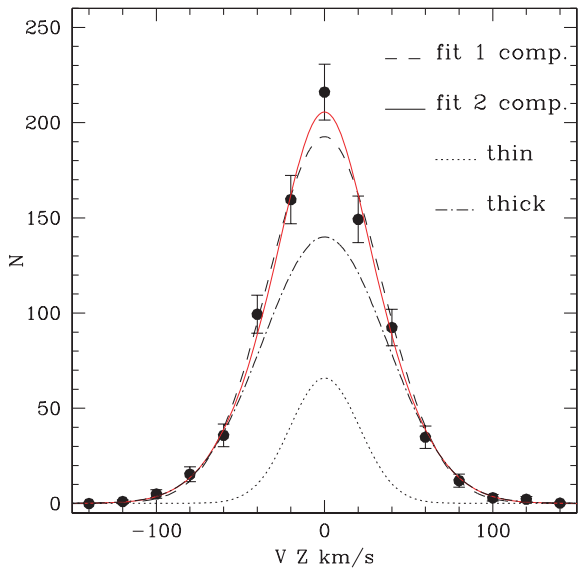

Figure 17. Example of decomposition of the vertical velocity distribution into a cold component (associated to the remnant thin disc) and a hot one (the thick disc). The normalization of each component has been fixed according to the photometric decomposition of Section 3.4.2.1 (see text). The contribution of the two components is shown separately.

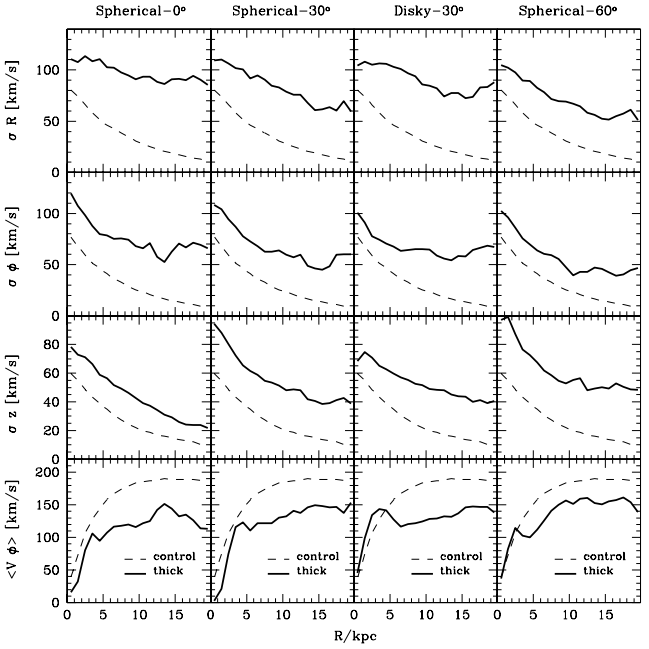

Figure 18. Final dynamical properties of the thick disc components for our prograde '$z = 0$' experiments. These properties have been computed at $t =$ 5 Gyr for stars within $|\mathcal{Z}| < 3$ kpc in concentric rings of 1 kpc width, using the decomposition described in Section 3.4.2.1. As reference, the final state of the disc in the control model is also shown (dashed).

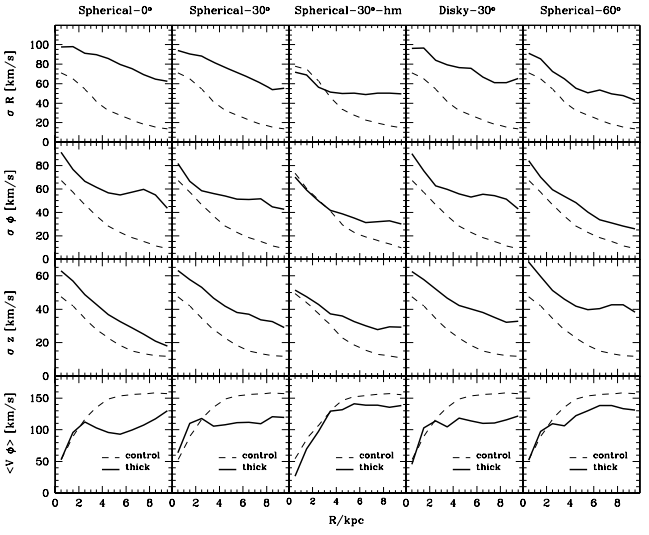

Figure 19. Final dynamical properties of thick disc components for our prograde '$z = 1$' experiments. The column 'hm' shows the satellite with half the mass. As in the previous figure, the properties have been computed within concentric rings of 1 kpc width, now for particles with $|\mathcal{Z}| < 1.5$ kpc at $t = 4$ Gyr (except for the 'hm' satellite, where $t = 6$ Gyr). The final state of the disc in the control model is shown by the dashed curves.

the radial velocity dispersions are generally larger by 5–10 km s^{-1} at all radii.

Figs 18 and 19 show that the radial σ_R and azimuthal σ_ϕ velocity dispersions of the thicker component are larger for lower inclination orbits moving in the prograde sense. The opposite trend is observed for the vertical velocity dispersion $\sigma_\mathcal{Z}$. This is as expected given our previous discussion on the evolution of the scaleheights and scalelengths and their dependence on orbital inclination. Spherical and discy satellites give rise to similar velocity distributions.

The resulting velocity dispersions σ_R and $\sigma_\mathcal{Z}$ for retrograde orbits are similar to the prograde cases. On the other hand, the azimuthal velocity distributions of the heated disc stars generally require an additional component to account for the contribution of the (accreted) counter-rotating stars (Villalobos & Helmi, in preparation). The global velocity dispersion (that would be obtained by imposing a single Gaussian for the thick component) would be in this case significantly larger at large radii for retrograde orbits, except for those with high inclination.

In general, the mean rotational velocities $\overline{v_\phi}$ of the thick discs differ noticeably from the coeval control simulation in all cases, by dropping $\sim$60 km s^{-1} although with a mild dependence on the orbital inclination. Low inclination encounters produce thick discs that rotate slower, implying larger asymmetric drifts. This is also evidenced by their larger radial and azimuthal velocity dispersions, as discussed above. The mean rotational velocity of thick discs which are the result of encounters with satellites on counter-rotating orbits is lower due to the contribution of the accreted stars, particularly at large radii.

The mean rotational velocity also shows noticeable differences with inclination when it is measured away from the mid-plane of the thick disc. In Fig. 20 we plot $\overline{v_\phi}$ for the prograde experiments at different heights above the plane, without making a distinction between the thin and thick disc components. Note that for $|\mathcal{Z}| >$ 1 kpc we are really measuring the kinematics of the thick disc component since the contribution of the remnant thin disc is negligible. Satellites with lower initial orbital inclinations induce a rotational lag, whose magnitude increases with height above the plane. This is because such satellites are more efficient in heating the disc radially at every height, leading to a larger asymmetric drift.

In Fig. 21 we plot the ratio $\sigma_\mathcal{Z}/\sigma_R$ of the thick disc component as a function of radius for different prograde experiments. Recall that the initial (and the control) disc has a (nearly) constant $\sigma_\mathcal{Z}/\sigma_R \sim 0.7$. This figure clearly shows that $\sigma_\mathcal{Z}/\sigma_R$ can be used as a discriminant of the initial inclination of the satellite. The reason for this strong dependence on inclination is essentially due the fact that a satellite on a highly inclined orbit will induce a much larger change in $\sigma_\mathcal{Z}$ at large radii than one on a coplanar orbit.

4 DISCUSSION

Previous works investigating the response of a host disc galaxy to one or more infalling satellites provide us with a valuable description of the dynamical effects involved in the process (QG86; Tóth & Ostriker 1992; QHF93; WMH96; HC97; VW99; Benson et al. 2004). HC97 find that a massive satellite (30 per cent of $M_{\rm disc}$), as it decays due to dynamical friction, can tilt the orientation of the disc up to 10° and cause warping. These effects illustrate the strong transfer of angular momentum from the infalling satellite to the host disc. VW99 note that satellites in prograde orbits mostly increase the disc heating. On the other hand, retrograde orbits are more efficient in tilting the disc orientation. Benson et al. (2004) show that more massive and more concentrated satellites increase the difference between the amount of disc heating caused by prograde and retrograde orbits. QG86 indicate that most of the kinetic energy of the infalling satellite is deposited on the plane of the disc and a small quantity heats up the vertical motions of disc particles. This shows that velocity dispersions in the host disc are not increased isotropically by the satellite. QHF93 note that most of the heating

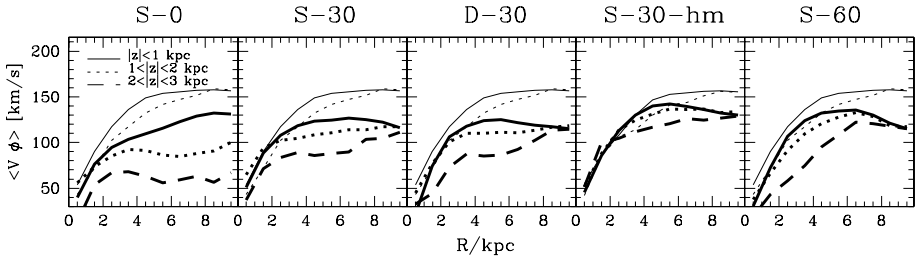

Figure 20. Mean azimuthal velocities of the 'stars' in our experiments at several heights above the plane as a function of radius for our '$z = 1$' experiments in prograde orbits. Thick lines include particles from both the heated disc and satellite, while the thin lines correspond to the disc in the control model (the highest $\mathcal{Z}$ range is not shown in this case because there are too few disc particles at that distance from the mid-plane). The same behaviour is observed in our '$z = 0$' experiments (not shown).

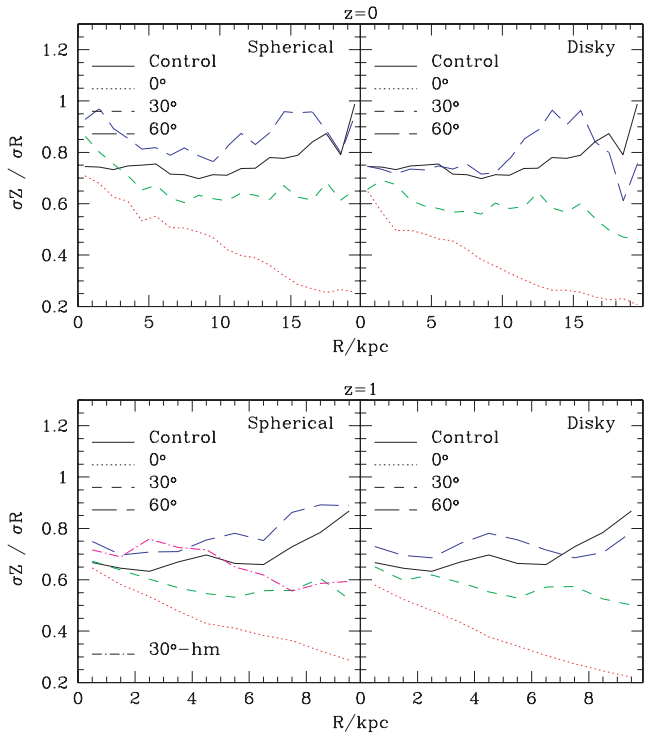

Figure 21. Final $\sigma_{\mathcal{Z}}/\sigma_R$ of thick remnants as a function of distance on the plane for different initial stellar distributions and orbital inclinations of the satellites. The control discs have a steady $\sigma_{\mathcal{Z}}/\sigma_R \sim 0.7$. Only prograde orbits are shown.

on the plane of the disc is caused by spiral arms stimulated by the decaying satellite. These arms also transfer angular momentum radially outwards, expanding the disc. QG86 and QHF93 also show that the vertical structure of the disc is not uniform across the disc. Instead, the scaleheight of the host discs increases at larger radii. Our simulations are not only able to confirm most of the aforementioned dynamical effects but also show a significantly larger tilting than previously found, both for the prograde and retrograde cases. This can be traced back to the fact that in our experiments, the accreted satellite is initially much more massive and is launched from a significantly larger distance (see Section 3.3).

4.1 Choice of massive satellites to heat discs up

Cosmological simulations show that massive mergers like those in our '$z = 1$' experiments are likely to have happened during the lifetime of a Milky Way sized host system. For instance, Kazantzidis et al. (2007) estimate the number of massive subhaloes accreted since $z \sim 1$ as at least one object with a mass $\sim M_{\rm disc}$ and five objects more massive than 20 per cent $M_{\rm disc}$. This is consistent with simulations by other groups (e.g. Stoehr 2006; De Lucia & Helmi 2008), and supported by the detailed study by Stewart et al. (2007). Even though massive mergers may be less frequent they are able to reach the centre of the host system thanks to dynamical friction, causing important changes in the structure and kinematics of the host disc. In principle, this could imply that a Milky Way like disc would experience only one severe change of orientation since $z \sim 1$ and also that only one massive satellite would be needed to heat up a pre-existing disc to give rise to a thick disc.

4.2 Observations of thick discs

Pohlen et al. (2004) have carried out photometric thick/thin disc decompositions and characterized properties such as scalelength and scaleheight for a sample of eight S0 edge-on galaxies by fitting three-dimensional (3D) disc models. The authors find that the mean scaleheight of the thick disc is between 2.4 and 5.3 times larger than that of the thin disc; while the mean scalelength is about twice, ranging from 1.6 to 2.6. In general these values are consistent the results obtained by other authors for S0, Sab, Sb, Sbc, Scd and Sd galaxies (e.g. van der Kruit 1984; de Grijs & van der Kruit 1996; de Grijs & Peletier 1997; Pohlen et al. 2004; Yoachim & Dalcanton 2006), including the Milky Way (Ojha 2001; Larsen & Humphreys 2003). *If* we assume that the structure of our simulated discs are not strongly affected by the formation of a new thin disc, *and* that these new thin discs will follow the same distribution as the remnant thin discs in our models, we can take the ratio of scaleheights obtained for our experiments at the final time at face value. Typically there is an increase in the scaleheight by a factor of 3–6, while the scalelengths are only slightly larger (with final-to-initial ratios between 1 and 1.4). These values appear to be in agreement with the range of ratios observed in general in spiral galaxies. However, this should be taken with great care because of the strong assumptions just made.

Most of our thick discs are significantly flared in the outer regions. This has also been found in other studies (e.g. Kazantzidis et al. 2007; Read et al. 2008), with varying strengths, depending on the initial configuration of the system. For example, galaxies with a bulge or embedded in a cored DM halo are more stable, and suffer from less flaring (Naab & Burkert 2003; Bournaud et al. 2005; Kazantzidis et al. 2007). This implies that we might expect to find in nature thick discs with varying degrees of flaring. However, quantifying this requires reaching extremely low surface brightness levels,

approximately 6–7 mag below the peak brightness of the *thick* disc. This is very challenging and has not yet been achieved in studies of surface photometry, which typically reach about 5 mag below the peak value of the *thin+thick* discs. For example, Neeser et al (2002) detected a thick disc in a low surface brightness galaxy. They reach a surface brightness level in the R band of 29 mag arcsec^{-2}. This is almost 7 mag below the central thin+thick disc value, and a very marginal indication of a flare is apparent on the east side of the thick disc at a distance of $\sim$3 scalelengths. Morrison et al. (1997) in their study of NGC 891 (a late-type disc with a small bulge) do not find evidence for flaring in the thick disc, but 'only' reach down to 26 mag arcsec^{-2} in R, which is about 6 mag below the central surface brightness of the dominant disc component.

DB02 have found a vertical colour gradient in their sample of galaxies, in the sense that the thick discs are redder, and consistent with a relatively old (>6 Gyr) stellar population. In the scenario we envisage for the formation of thick discs we would expect two sources of colour gradients. The first would be due to the transition from the population of young thin disc stars to the thick disc stars formed *in situ*, i.e. originating from a pre-existing thin disc. Unfortunately, because we do not model the formation of a new disc from freshly accreted gas, we cannot make a quantitative comparison. The second source of a change in stellar populations would be due to the difference between accreted satellite stars and those formed *in situ* in the (heated) disc. Our Figs 15 and 16 show that the fraction of satellite particles is generally quite low. Only at distances above the plane of approximately six thick disc scaleheights, the number of accreted stars is comparable to that of the heated disc. This implies that this second gradient should be weaker, and is unlikely to be detected in current observations because at these heights, the typical surface brightness levels are exceedingly low (see Fig. 11).

Kinematically, the values of the velocity ellipsoids of our thick discs, measured at $R \approx 2.4R_{\rm D}$, are in good agreement with the one observed at the solar radius in the Milky Way ($\sigma_R, \sigma_\phi, \sigma_z$) $\sim$ (65, 54, 38) km s^{-1} (e.g. see Layden et al. 1996; Chiba & Beers 2001; Soubiran et al. 2003; Alcobé & Cubarsi 2005; Vallenari et al. 2006; Veltz et al. 2008). The values of σ_z/σ_R measured by most of these authors are typically $\sim$0.6,[4] suggesting that the thick disc of the Galaxy could have been produced by a merger of intermediate inclination (see Fig. 21). The differences between the mean rotational velocity of the final thick disc and that of the remnant thin disc are $\Delta\overline{v_\phi} \sim$ 40–50 km s^{-1}. Note that these values cannot be interpreted directly as the observed rotational lag between the thin and thick discs in the Milky Way since we do not include gas in our simulations that later on can collapse and actually form a new thin disc (see Section 4.4.1).

4.3 Our simulations in the context of M31

It is important to notice that in our experiments configured at '$z = 0$' the initial properties of the host disc, before the merger with the satellite, resemble the properties of the current thin disc of the Galaxy. This implies that the final thick discs generated in our experiments are too massive and do not represent direct analogues of the thick disc of the Milky Way. However, this set of simulations may be useful for understanding the evolution of M31, which is likely to have experienced recent merger events as may be inferred from the rich and complex structures present in its outskirts (Ibata et al. 2007, and references therein).

For example, Ibata et al. (2005) discovered an extended and clumpy disc-like structure around M31 with a scalelength similar to that of the main disc, rotating $\sim$40 km s^{-1} slower and with a rather low velocity dispersion of $\sim$30 km s^{-1}. Its stellar population has homogeneous kinematics and abundances over the entire region where it is observed, which suggests that it was formed in a single global event. However, it is not straightforward to link the extended disc of M31 to the thick disc modelled here, mainly because of the much higher velocity dispersions of the final thick discs in our simulations.

The giant stream of M31, thought to originate in the disruption of a satellite with mass $\sim 10^9$ M$_\odot$, and the so-called eastern and western 'shelfs' (Ibata et al. 2007), may be related given the similarities of their stellar populations. In the context of our simulations, this would be quite natural. Analogous structures are observed as the satellite is disrupted as shown in Figs 5 and 6 for prograde orbits in face-on view at 1.5 Gyr (see also Fardal et al. 2007; Mori & Rich 2008). It is interesting to note that much sharper and longer lasting shells are generated by discy satellites compared to spherical ones.

4.4 Caveats

4.4.1 Lack of gas physics in our simulations

In this paper we have focused on the collisionless interactions between a disc galaxy and a satellite, with both DM and stellar components, without including gas physics or star formation which may affect the interactions and the final thick disc's properties. This is potentially the most crucial simplifying assumption in this study since disc galaxies were presumably much more gas rich at high redshift (Robertson et al. 2006).

The lack of gas physics implies that the modelled discs do not grow in stellar mass or in size during the time-span of the merger (except of course through the dynamical heating processes described above). Furthermore, it is likely that such mergers would trigger a (strong) burst of star formation. These new stars would be relatively old at the present day and located in a thinner structure. On the other hand, some orbital energy deposited by the infalling satellite into the gas could be radiated away from the system, reducing the dynamical damage done to the disc (QHF93). For example, in recent work Hopkins et al. (2008) based on Younger et al. (2008) suggested that the change in the structural parameters depends on the fraction of gas $f_{\rm g}$ available as $\delta H \sim (1 - f_{\rm g})\delta H_*$, where δH_* corresponds to the scale change in the purely dissipationless case.

Any remaining (and presumably heated) gas would eventually cool and settle down to form a new thin disc. This slow accumulation of gas on the mid-plane should induce a contraction of the thick disc. For example, Elmegreen & Elmegreen (2006) estimate that this contraction leads to a decrease in the scaleheight of the contracted thick by $\sim$40 per cent and an increase of the velocity dispersion by $\sim$50 per cent. Furthermore, the accretion of fresh gas from the intergalactic medium is likely to also be important, and will lead to further changes to the properties of the merger products studied here.

4.4.2 Time dependence of gravitational potential

In general, the structure of a DM halo evolves with time through mergers and slow accretion. However, in our simulations we have neglected any cosmological evolution of the structure of the host

[4] Although Veltz et al. find $\sigma_z/\sigma_R \sim 0.9$, which could be due to the fact that the assumption of isothermality for the velocity distribution is not valid.

halo during and after the merger with the satellite. This simplification may be justified by recent studies (e.g. Wechsler et al. 2002; Romano-Diaz et al. 2006), which have shown that the structure of dark haloes is very stable within the scale radius r_s after the phase of active mergers, which for a disc galaxy must have ended at redshifts ∼0.5–1. This is indeed the region that we follow dynamically in our simulations, after the initial decay of the satellite due to dynamical friction, which lasts typically less than 1 Gyr. Therefore, the final thick discs are well within this scale radius, being $r_s \sim 6$ and ∼11 times the final scalelengths in the '$z = 0$' and '$z = 1$' experiments, respectively.

5 SUMMARY AND CONCLUSIONS

We have performed numerical simulations of the heating of a disc galaxy by a single relatively massive merger. These mergers lead to the formation of thick discs whose characteristics are similar, both in morphology as in kinematics, to those observed in the Milky Way and other spiral galaxies.

The simulations explore several configurations of the progenitor systems whose properties have been scaled at two different redshifts in order to study the formation of thick discs at different epochs. The satellites have total masses of 10 and 20 per cent that of the host galaxy and have been modelled self-consistently as a stellar component immersed in a DM halo. The stellar components have either a spherical or discy distribution. The satellites have been released far away from the host disc, with initial orbital parameters that are consistent with cosmological studies. Additionally, three different initial orbital inclinations of the satellites have been studied in both prograde and retrograde directions with respect to the rotation of the host disc.

We find that as the satellite galaxies spiral in through dynamical friction, significant asymmetries are visible, both in the host disc and in the satellite debris. Particularly interesting are the low surface brightness shells, especially visible in the outskirts of the final thick discs, that last for about 1.5 to 2 Gyr after the merger has been completed. These shells acquire relevance in the case of Andromeda where according to recent studies a couple of these features are likely associated to the event that also gave rise to the giant stream (Ibata et al. 2007, and references therein).

Despite the relatively large mass ratios, the infalling satellites do not fully destroy the host disc, but merely heat it and tilt it. The host discs are found to change their orientation both for the prograde and retrograde encounters. Furthermore, a remnant thin component containing between 15 and 25 per cent of the total stellar mass of the system is present at the final time in all our experiments. This prediction of the minor merger model might be potentially relevant to understand the presence of a very old thin disc in the Milky Way.

The scalelengths of the final thick discs are slightly more extended than those of the original host disc while the scaleheights are between three and six times larger, depending on the initial inclination of the satellite. The scaleheights have also increased in proportion to the inclination of the encounter, and the outer discs are noticeably flared. If this is the case for the thick disc of the Milky Way, part of the flared material could be (confused with) the Monoceros ring.

In our simulations, the outer isophotes of the final thick discs (measured at surface brightness levels >6 mag below the central value) are consistently more boxy than the inner ones. The eventual detection of such degree of boxiness, especially for bulgeless galaxies, would provide support for a formation process as that modelled here.

Interestingly, the fraction of satellite particles at a given galactic radius as a function of height above the plane, when normalized by the (luminosity-weighted) scaleheight, *only* depends on the mass ratio between the satellite and host and not on stellar morphology of the satellite or type of orbit. For instance, at a distance of four scaleheights the fraction of satellite particles reflects the mass ratio of the merger.

We find that satellite stars do not dominate the luminosity of the thick disc until rather far above the mid-plane. In this sense, the existence of a counter-rotating thick disc, detected by Yoachim & Dalcanton (2005) only ∼two thick-disc scaleheights above the mid-plane, can only be explained in the context of our models if the (young) thin disc formed from freshly accreted counter-rotating gas. The remaining possibility is, of course, that the thick disc formed exclusively by direct accretion of stars from an infalling satellite. Relatively fast rotating thick discs (like the one of the Milky Way) may be more easily explained by disc heating formation, since a random distribution of accreted satellites would seem to have less chance of producing thick discs with strong coherent rotation.

If taken at face value the velocity ellipsoids of the simulated thick discs are in good agreement with observations of the Galactic thick disc at the solar radius. The rotational lag may also be consistent with observations. These statements are however only valid if we neglect further significant evolution due to the formation of a thin disc component from freshly accreted gas. The observed trend of the ratio σ_z/σ_R with radius in the final thick discs is found to be a very good discriminant of the initial inclination of the decaying satellite. In the case of the Milky Way, the observed σ_z/σ_R at the position of the Sun is ∼0.6 (e.g. Chiba & Beers 2001; Vallenari et al. 2006), suggesting that the thick disc of the Galaxy could have been produced by a merger of intermediate inclination. Measurements of the mean rotational velocity in the final thick discs, at several heights from the mid-plane, indicate that satellites with lower initial inclinations are more efficient in introducing asymmetric drifts dependent on height. This implies that the possible existence of vertical gradients in the mean rotational velocity in the thick disc of the Galaxy (Girard et al. 2006) would also favour mergers with either low or intermediate orbital inclination. We defer to Paper II a more detailed analysis of the phase-space structure of the merger product. We expect this will lead to new constrains on the mechanism described here for the formation of the Galactic thick disc.

ACKNOWLEDGMENTS

We are grateful to the referee for the extensive and very insightful comments which have led to a number of significant improvements in our manuscript. We thank M. C. Smith and L. Sales for stimulating discussions and suggestions, and S. C. Trager and R. Sanders for useful remarks. We acknowledge financial support from the Netherlands Organisation for Scientific Research (NWO). The simulations were run in the Linux cluster at the Centre for High Performance Computing and Visualisation (HPC/V) of the University of Groningen in the Netherlands.

REFERENCES

Abadi M. G., Navarro J. F., Steinmetz M., Eke V. R., 2003, ApJ, 597, 21
Aguerri J. A. L., Balcells M., Peletier R. F., 2001, A&A, 367, 428
Alcobé S., Cubarsi R., 2005, A&A, 442, 929
Ardi E., Tsuchiya T., Burkert A., 2003, ApJ, 596, 204

Athanassoula E., Fady E., Lambert J. C., Bosma A., 2000, MNRAS, 314, 475
Athanassoula E., Lambert J. C., Dehnen W., 2005, MNRAS, 363, 496
Bekki K., Chiba M., 2001, ApJ, 558, 666
Bender R., Doebereiner S., Moellenhoff C., 1988, A&AS, 74, 385
Benson A. J., 2005, MNRAS, 358, 551
Benson A. J., Lacey C. G., Frenk C. S., Baugh C. M., Cole S., 2004, MNRAS, 351, 1215
Berentzen I., Athanassoula E., Heller C. H., Fricke K. J., 2004, MNRAS, 347, 220
Binney J., Tremaine S., 1987, Galactic Dynamics. Princeton Univ. Press, Princeton, NJ
Blumenthal G. R., Faber S. M., Flores R., Primack J. R., 1986, ApJ, 301, 27
Bournaud F., Jog C. J., Combes F., 2005, A&A, 437, 69
Bournaud F., Elmegreen B. G., Elmegreen D. M., 2007a, ApJ, 670, 237
Bournaud F., Jog C. J., Combes F., 2007b, A&A, 476, 1179
Brook C. B., Kawata D., Gibson B. K., Freeman K. C., 2004, ApJ, 612, 894
Brook C. B., Gibson B. K., Martel H., Kawata D., 2005, ApJ, 630, 298
Burkert A., Truran J. W., Hensler G., 1992, ApJ, 391, 651
Burstein D., 1979, ApJ, 234, 829
Chen B., the SDSS Collaboration, 2001, ApJ, 553, 184
Chiba M., Beers T. C., 2001, ApJ, 549, 325
Cox T. J., Younger J., Hernquist L., Hopkins P. F., 2008, in Bureau M., Athanassoula E., Barbuy B., eds, IAU Symp. Vol. 245, Formation and Evolution of Galaxy Bulges. Cambridge Univ. Press, Cambridge, p. 63
Dalcanton J. J., Bernstein R. A., 2000, AJ, 120, 203
Dalcanton J. J., Bernstein R. A., 2002, AJ, 124, 1328 (DB02)
de Grijs R., Peletier R. F., 1997, A&A, 320, L21
de Grijs R., van der Kruit P. C., 1996, A&AS, 117, 19
De Lucia G., Helmi A., 2008, MNRAS, in press (arXiv:0804.2465)
de Rijcke S., Michielsen D., Dejonghe H., Zeilinger W. W., Hau G. K. T., 2005, A&A, 438, 491
di Matteo P., Combes F., Melchior A.-L., Semelin B., 2007, A&A, 468, 61
Eggen O. J., Lynden-Bell D., Sandage A. R., 1962, ApJ, 136, 748
Elmegreen B. G., Elmegreen D. M., 2006, ApJ, 650, 644
Fardal M. A., Guhathakurta P., Babul A., McConnachie A. W., 2007, MNRAS, 380, 15
Font A. S., Navarro J. F., Stadel J., Quinn T., 2001, ApJ, 563, L1
Freeman K., Bland-Hawthorn J., 2002, ARA&A, 40, 487
Fuhrmann K., 2004, Astron. Nachr., 325, 3
Gauthier J.-R., Dubinski J., Widrow L. M., 2006, ApJ, 653, 1180
Gilmore G., Reid N., 1983, MNRAS, 202, 1025
Gilmore G., Wyse R. F. G., 1986, Nat, 322, 806
Gilmore G., Wyse R. F. G., Norris J. E., 2002, ApJ, 574, L39
Girard T. M., Korchagin V. I., Casetti-Dinescu D. I., van Altena W. F., López C. E., Monet D. G., 2006, AJ, 132, 1768
Hayashi H., Chiba M., 2006, PASJ, 58, 835
Helmi A., Navarro J. F., Meza A., Steinmetz M., Eke V. R., 2003, ApJ, 592, L25
Helmi A., Navarro J. F., Nordström B., Holmberg J., Abadi M. G., Steinmetz M., 2006, MNRAS, 365, 1309
Hernquist L., 1990, ApJ, 356, 359
Hernquist L., 1993, ApJS, 86, 389
Hernquist L., Quinn P. J., 1988, ApJ, 331, 682
Hernquist L., Quinn P. J., 1989, ApJ, 342, 1
Hopkins P. F., Hernquist L., Cox T. J., Younger J. D., Besla G., 2008, ApJ, in press (arXiv:0806.2861)
Huang S., Carlberg R. G., 1997, ApJ, 480, 503 (HC97)
Ibata R., Chapman S., Ferguson A. M. N., Lewis G., Irwin M., Tanvir N., 2005, ApJ, 634, 287
Ibata R., Martin N. F., Irwin M., Chapman S., Ferguson A. M. N., Lewis G. F., McConnachie A. W., 2007, ApJ, 671, 1591
Jedrzejewski R. I., 1987, MNRAS, 226, 747
Jensen E. B., Thuan T. X., 1982, ApJS, 50, 421
Jesseit R., Naab T., Burkert A., 2005, MNRAS, 360, 1185
Kazantzidis S., Magorrian J., Moore B., 2004, ApJ, 601, 37
Kazantzidis S., Bullock J. S., Zentner A. R., Kravtsov A. V., Moustakas L. A., 2007, ApJ, in press (arXiv:0708.1949)
Khochfar S., Burkert A., 2006, A&A, 445, 403
Kregel M., van der Kruit P. C., de Grijs R., 2002, MNRAS, 334, 646
Kroupa P., 2002, MNRAS, 330, 707
Larsen J. A., Humphreys R. M., 2003, AJ, 125, 1958
Layden A. C., Hanson R. B., Hawley S. L., Klemola A. R., Hanley C. J., 1996, AJ, 112, 2110
Lewis J. R., Freeman K. C., 1989, AJ, 97, 139
Martin N. F., Ibata R. A., Bellazzini M., Irwin M. J., Lewis G. F., Dehnen W., 2004, MNRAS, 348, 12
Mihos J. C., Walker I. R., Hernquist L., Mendes de Oliveira C., Bolte M., 1995, ApJ, 447, L87
Mo H. J., Mao S., White S. D. M., 1998, MNRAS, 295, 319
Mori M., Rich R. M., 2008, ApJ, 674, L77
Morrison H. L., Miller E. D., Harding P., Stinebring D. R., Boroson T. A., 1997, AJ, 113, 2061
Mould J., 2005, AJ, 129, 698
Naab T., Burkert A., 2003, ApJ, 597, 893
Naab T., Trujillo I., 2006, MNRAS, 369, 625
Naab T., Jesseit R., Burkert A., 2006, MNRAS, 372, 839
Navarro J. F., Frenk C. S., White S. D. M., 1997, ApJ, 490, 493 (NFW)
Navarro J. F., Helmi A., Freeman K. C., 2004, ApJ, 601, L43
Norris J. E., Ryan S. G., 1991, ApJ, 380, 403
Ojha D. K., 2001, MNRAS, 322, 426
Pardi M. C., Ferrini F., Matteucci F., 1995, ApJ, 444, 207
Pohlen M., Dettmar R.-J., Lütticke R., Schwarzkopf U., 2000, A&AS, 144, 405
Pohlen M., Balcells M., Lütticke R., Dettmar R.-J., 2004, A&A, 422, 465
Press W. H., Teukolsky S. A., Vetterling W. T., Flannery B. P., 1992, Numerical Recipes in C. The Art of Scientific Computing, 2nd edn. Cambridge Univ. Press, Cambridge
Quinn P. J., Goodman J., 1986, ApJ, 309, 472 (QG86)
Quinn P. J., Hernquist L., Fullagar D. P., 1993, ApJ, 403, 74
Read J. I., Lake G., Agertz O., Debattista V. P., 2008, MNRAS, 389, 1041
Robertson B., Bullock J. S., Cox T. J., Di Matteo T., Hernquist L., Springel V., Yoshida N., 2006, ApJ, 645, 986
Robin A. C., Haywood M., Creze M., Ojha D. K., Bienayme O., 1996, A&A, 305, 125
Romano-Diaz E., Faltenbacher A., Jones D., Heller C., Hoffman Y., Shlosman I., 2006, ApJ, 637, L93
Sellwood J. A., 1987, ARA&A, 25, 151
Sellwood J. A., Nelson R. W., Tremaine S., 1998, ApJ, 506, 590
Seth A. C., Dalcanton J. J., de Jong R. S., 2005, AJ, 130, 1574
Soubiran C., Bienaymé O., Siebert A., 2003, A&A, 398, 141
Springel V., 2005, MNRAS, 364, 1105
Springel V., White S. D. M., 1999, MNRAS, 307, 162
Stewart K. R., Bullock J. S., Wechsler R. H., Maller A. H., Zentner A. R., 2008, ApJ, 683, 597
Stoehr F., 2006, MNRAS, 365, 147
Toomre A., 1964, ApJ, 139, 1217
Tormen G., 1997, MNRAS, 290, 411
Tóth G., Ostriker J. P., 1992, ApJ, 389, 5
Tsikoudi V., 1979, ApJ, 234, 842
Vallenari A., Pasetto S., Bertelli G., Chiosi C., Spagna A., Lattanzi M., 2006, A&A, 451, 125
van der Kruit P. C., 1984, A&A, 140, 470
van der Kruit P. C., Searle L., 1981a, A&A, 95, 105
van der Kruit P. C., Searle L., 1981b, A&A, 95, 116
van Dokkum P. G., Peletier R. F., de Grijs R., Balcells M., 1994, A&A, 286, 415
Velázquez H., White S. D. M., 1999, MNRAS, 304, 254 (VW99)
Veltz L. et al., 2008, A&A, 480, 753
Walker I. R., Mihos J. C., Hernquist L., 1996, ApJ, 460, 121 (WMH96)
Wechsler R. H., Bullock J. S., Primack J. R., Kravtsov A. V., Dekel A., 2002, ApJ, 568, 52
Yoachim P., Dalcanton J. J., 2005, ApJ, 624, 701
Yoachim P., Dalcanton J. J., 2006, AJ, 131, 226
Younger J. D., Besla G., Cox T. J., Hernquist L., Robertson B., Willman B., 2008, ApJ, 676, L21

APPENDIX A: SETTING UP THE INITIAL CONDITIONS FOR THE HOST AND SATELLITE SYSTEMS

A1 Main disc galaxy

The main disc galaxy is a self-consistent two-component system, containing a DM halo and a stellar disc.

A1.1 Dark matter halo

The DM haloes in our simulations follow a NFW mass density profile (NFW):

$$\rho_{\rm NFW}(r) = \frac{\rho_{\rm s}}{(r/r_{\rm s})\,(1 + r/r_{\rm s})^2}, \tag{A1}$$

where $\rho_{\rm s}$ is a characteristic scale density and $r_{\rm s}$ a scale radius. The advantage of using this density profile is that it is consistent with cosmological simulations, and its evolution with redshift (or time) is relatively well known (e.g. Wechsler et al. 2002). This implies that it is easy to rescale its properties to study the formation of thick discs at redshifts greater than zero.

In this paper we adopt a flat cosmology defined by $\Omega_{\rm m}(z = 0) = 0.3$ and $\Omega_\Lambda = 0.7$ with a Hubble constant of $H(z = 0) = 70\,{\rm km\,s^{-1}\,Mpc^{-1}}$.

The virial radius of the halo $R_{\rm vir}(z)$ is defined as the radius within which the mean density is $\Delta_{\rm vir}(z)$ times the critical density $\rho_{\rm c}(z)$ of the universe at a given redshift:

$$M_{\rm vir}(z) = \frac{4\pi}{3}\Delta_{\rm vir}(z)\rho_{\rm c}(z)R_{\rm vir}^3, \tag{A2}$$

where the virial overdensity $\Delta_{\rm vir}(z)$ is taken from the solution to the dissipationless collapse in the spherical top-hat model. Its value is $18\pi^2$ for a critical universe but has a dependency on cosmology. In the case of flat cosmologies, $\Delta_{\rm vir}(z) \approx (18\,\pi^2 + 82x + 39x^2)$, where $x = \Omega(z) - 1$, and $\Omega(z)$ is defined as the ratio between mean matter density and critical density at redshift z. Another important related quantity is the concentration c defined as $c = R_{\rm vir}/r_{\rm s}$. From Wechsler et al. (2002) we take the relation linking $M_{\rm vir}$ to the concentration parameter c at redshift $z = 0$ as

$$c \simeq 20\left(\frac{M_{\rm vir}}{10^{11}\,{\rm M}_\odot}\right)^{-0.13}. \tag{A3}$$

We follow Wechsler et al. (2002) to scale both the virial mass of the halo and its concentration as a function of redshift:

$$M_{\rm vir}(z) = M_{\rm vir}(z = 0)\exp(-2a_{\rm c}z), \tag{A4}$$

$$c(z) = \frac{c(z = 0)}{1 + z}, \tag{A5}$$

where $a_{\rm c}$ is a constant defined as the formation epoch of the halo, taken as $a_{\rm c} = 0.34$. In practice this means that the structure of the halo of the main galaxy at any redshift is fully determined by imposing only a value for the virial mass at redshift $z = 0$. The values of the halo parameters used in our simulations are included in the Table 1.

Since the mass of a NFW profile formally diverges with radius, we introduce an exponential truncation starting at $R_{\rm vir}$ and decaying on a scale $r_{\rm dec}$ (Springel & White 1999):

$$\rho(r) = \frac{\rho_{\rm s}}{c(1 + c)^2}\left(\frac{r}{R_{\rm vir}}\right)^{\epsilon}\exp\left(-\frac{r - R_{\rm vir}}{r_{\rm dec}}\right)(r > R_{\rm vir}), \tag{A6}$$

where $r_{\rm dec}$ is a free parameter. By requiring continuity at $R_{\rm vir}$ between equations (A1) and (A6), and also between their logarithmic slopes, the exponent ϵ is computed as

$$\epsilon = -\frac{1 - 3c}{1 + c} + \frac{R_{\rm vir}}{r_{\rm dec}}. \tag{A7}$$

Note that for $r_{\rm dec} = 0.1\ R_{\rm vir}$ the total mass of the halo becomes $\sim$10 per cent larger than $M_{\rm vir}$. We define the maximum extension of the halo as $R_{\rm max} = R_{\rm vir} + 3\ r_{\rm dec}$.

We also allow the contraction of the halo in response to the formation of a stellar disc in its central part (Blumenthal et al. 1986; Mo et al. 1998). The adiabatic contraction first assumes that the gas (that later forms the disc/bulge) is distributed in the same way as the DM. Then both the spherical symmetry of the halo and also the angular momentum of each DM orbit are conserved during the contraction, i.e.

$$r_{\rm i}M_{\rm i}(r_{\rm i}) = r_{\rm f}M_{\rm f}(r_{\rm f}), \tag{A8}$$

where $r_{\rm i}$ and $r_{\rm f}$ are the initial and final radius of a shell of DM, $M_{\rm i}$ is the initial total mass (distributed according to an NFW profile) and $M_{\rm f}$ is the mass distribution after the disc has been formed, and also includes the contribution of the disc. Therefore,

$$M_{\rm f}(r_{\rm f}) = M_{\rm d}(r_{\rm f}) + (1 - m_{\rm d})M_{\rm i}(r_{\rm i}), \tag{A9}$$

where $m_{\rm d} = M_{\rm disc}/M_{\rm halo}$. The final DM distribution of the adiabatically concentrated halo will be

$$M_{\rm halo}(r) = M_{\rm f}(r) - M_{\rm disc}(r). \tag{A10}$$

Now that the mass distribution of the halo component has been defined, it is straightforward to initialize the positions of the particles in our haloes. As the next step, the velocity of each particle is computed from the distribution function (DF) associated to the adiabatically contracted mass density profile $\rho_{\rm halo}(r)$. We follow Kazantzidis, Magorrian & Moore (2004) and compute numerically the DF that, in general, is given by[5]

$$f(Q) = \frac{1}{\sqrt{8}\pi^2}\left[\int_0^Q \frac{{\rm d}^2\rho_{\rm halo}}{{\rm d}\psi^2}\frac{{\rm d}\psi}{\sqrt{Q - \psi}} + \frac{1}{\sqrt{Q}}\left(\frac{{\rm d}\rho_{\rm halo}}{{\rm d}\psi}\right)_{\psi=0}\right] \tag{A11}$$

(Binney & Tremaine 1987), where $Q = \psi - v^2/2; \psi = -\Phi(r)$ is the effective gravitational potential (including the disc) and v is the velocity of each particle. Finally, we use the rejection method (Press et al. 1992) to generate the velocities for our particles.

A1.2 Stellar disc

The disc component is constructed following the procedure outlined by Hernquist (1993) and QHF93 which consists, briefly, in initializing particle positions according to a density profile of the form

$$\rho_{\rm d}(R, \mathcal{Z}) = \frac{M_{\rm d}}{8\pi R_{\rm D}^2\mathcal{Z}_0}\exp\left(-\frac{R}{R_{\rm D}}\right)\,{\rm sech}^2\left(\frac{\mathcal{Z}}{2\mathcal{Z}_0}\right), \tag{A12}$$

where $M_{\rm d}$ is the disc mass, $R_{\rm D}$ is the exponential scalelength and $\mathcal{Z}_0$ is the exponential scaleheight.

The velocity components v_R, v_ϕ and $v_\mathcal{Z}$ of the disc particles are calculated from moment equations of the collisionless Boltzmann equation (CBE) supplemented by observational constraints (Binney

[5] For a spherical non-rotating system.

& Tremaine 1987). We assume that locally (at each point in the disc) the velocity distribution can be approximated by a Maxwellian, whose parameters are set up as follows.

(i) The radial velocity dispersion $\overline{v_{\rm R}^2}(R) \propto \exp(-R/R_{\rm D})$. This is motivated by observations of external galaxies (van der Kruit & Searle 1981a; Lewis & Freeman 1989). The normalization constant is set by adopting a certain value of the stability Q parameter (Toomre 1964) at a particular location in the disc. In this paper $Q = 2$ at $R = 2.4R_{\rm D}$, which for a Milky Way like disc corresponds to the solar radius.

(ii) The vertical velocity dispersion $\overline{v_{\mathcal{Z}}^2}(R) = 2\pi {\rm G}\Sigma(R)\mathcal{Z}_0$, following the isothermal sheet model.

(iii) The dispersion in the azimuthal direction is obtained by using the epicyclic approximation (Binney & Tremaine 1987) $\sigma_\phi^2(R) = \overline{v_R^2}(R)\kappa^2(R)/4\Omega^2(R)$, where κ and Ω are the epicyclic and angular frequencies, respectively. The mean values of the azimuthal Gaussian distributions are calculated from the second moment of the CBE:

$$\overline{v_\phi}^2(R) = \overline{v_R^2}(R)\left[1 - \frac{\kappa^2(R)}{4\Omega^2(R)} - 2\frac{R}{R_{\rm D}}\right] + v_{\rm c}^2(R),$$

where $v_{\rm c}(R) = R\,\Omega(R)$ is the circular velocity considering all the components of the system.

Note that velocities derived from the CBE are close but not identical to the ones derived from the DF of the disc. Unfortunately, the DF is unknown for the disc in equation (A12). Therefore, we can expect some initial evolution in the disc properties. As shown in Section A3, this evolution is indeed minimal.

A2 Numerical parameters

The N-body systems are evolved using GADGET-2.0 (Springel 2005) a well documented massively parallel TREESPH code. Depending on the system under study, this code has to be provided with suitable values for the so-called numerical parameters, being these the number of particles N to represent a given component in the system, the softening ϵ of gravitational forces to avoid strong artificial accelerations between particles passing close to each other and finally the time-step Δt, that controls the frequency at which positions and velocities are computed for each particle. In general, these three parameters set the mass, spatial and time resolution in a numerical simulation. At the moment of defining N, ϵ and Δt the usual problem is that they are interrelated in a complicated way. For instance, N will depend on the available CPU power to run the simulations; ϵ will depend on both N and the mass distribution of the system to be simulated and Δt will depend on the smallest spatial resolution that is possible to resolve, ϵ, and again on the available CPU power. The optimal choice of these parameters will establish a compromise between quality and efficiency in a numerical simulation.

A2.1 Number of particles

Tables 1 and 2 list the numbers of particles used for each component in our simulations. As shown by WMH96, using self-consistent simulations of an isolated halo–disc system, large numbers of particles in the halo are needed to suppress the formation of bar perturbations in the disc. This is because large $N_{\rm halo}$ decreases the graininess of the potential, which bars are seeded from. WMH96 suggest the use of $\sim$500 000 particles in the halo in order to smooth out the potential for time-scales comparable to the orbital decay of satellites in our simulations.

For our purposes, bars are an unwanted effect because they represent an additional source of disc heating, besides the one of interest here. Although the complete elimination of bar formation in a self-consistent simulation is difficult, its effect on the disc can be constrained by evolving the main disc galaxy in isolation, for the same time-scale as the merger simulation.

The number of particles in the host disc $N_{\rm host,disc} = 10^5$, and is similar to previous studies on disc heating by mergers with satellites. The satellites are modelled with a relatively large number of particles (particularly in comparison to previous works) to study the distribution of the debris, which is the focus of Paper II. In all cases we can follow accurately the structure and evolution of each component during the simulations.

A2.2 Softening

Many studies have been carried out on how to choose the optimal gravitational force softening ϵ in order to faithfully represent the system (see Sellwood 1987, for an excellent review). We use here the prescription by Athanassoula et al. (2000). These authors present a simple method to estimate ϵ for arbitrary mass distributions as a function of the number of particles. The optimal softening $\epsilon_{\rm opt}$ is the one that minimizes the error in the forces between particles in a system with a given mass distribution. They find a correlation between $\epsilon_{\rm opt}$ and the distance $r_{6,\rm mean}$ from every particle to its sixth closest neighbour, which is defined as

$$r_{6,\rm mean} = \left(N^{-1}\sum_{i=1}^{N} r_{6,i}^{-1}\right)^{-1}, \qquad \text{(A13)}$$

where $r_{6,\rm mean}$ depends on both the number of particles and the mass distribution. Fig. A1 shows $\epsilon_{\rm opt}$ as a function of $r_{6,\rm mean}$ for three mass distributions discussed by Athanassoula et al. (2000) in order of increasing density: homogeneous sphere, Plummer profile and Dehnen model (with $\gamma = 0$). To estimate the $\epsilon_{\rm opt}$ for the systems of our simulations the procedure followed is (1) compute $r_{6,\rm mean}$ for each of our components; (2) compare the central density of our components to the ones of the homogeneous, Plummer and Dehnen spheres. By doing so the optimal softening for each component can be constrained within a range on the plane r_6–$\epsilon_{\rm opt}$ and (3) $\epsilon_{\rm opt}$ is found by running a few simulations with a set of ϵ within this range and choosing the one that offers the best stability. Specifically, a softening is considered optimal when each component of both the host and satellite systems present the least evolution in their structure and kinematics (in the case of the host minimizing the effect of non-axisymmetries) during the amount of time required for the satellite to sink and become fully disrupted.

In Fig. A1 darker symbols show the adopted values of $\epsilon_{\rm opt}$ for each component at every redshift. Note that for each component the values of $\epsilon_{\rm opt}$ are well constrained on the r_6–$\epsilon_{\rm opt}$ plane, facilitating the extrapolation of these optimal values to similar systems with a different number of particles. For each component, the adopted values of $\epsilon_{\rm opt}$ are listed in Tables 1 and 2.

The distinctive location of the optimal softenings on the r_6–$\epsilon_{\rm opt}$ diagram basically depends on both the central concentration of the systems and on the number of particles used to model them. For instance, haloes of hosts and satellites at '$z = 0$' and '$z = 1$' always lie below the Dehnen model because they are more centrally concentrated (even more so when the adiabatic contraction is taken into account). On the other hand, the separation along the r_6 coordinate between the optimal softening of the haloes of hosts and satellites reflects the difference in the number of particles used to model them.

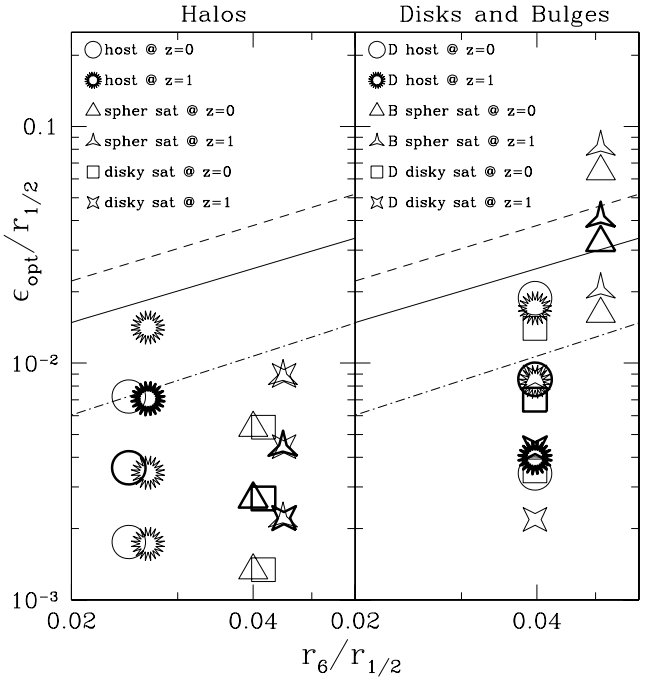

Figure A1. Numerical softening as a function of the mean distance from each particle to the sixth closest neighbour in units of the half-mass radius $r_{1/2}$. Straight lines are extrapolations towards smaller r_6 taken from the results of Athanassoula et al. (2000) [see fig. 11 in that work]. Dashed, solid and dot–dashed lines show the values for a homogeneous, Plummer and Dehnen sphere (with $\gamma = 0$), respectively. The symbols indicate the values of softenings explored in this paper for each component. Darker symbols show the optimal softenings that produced the best stability in each case.

In this sense it is easy to associate systems with a larger number of particles to smaller mean distances between particles and vice versa, given that the systems are compared in a normalized scale.

Also note that the discy satellite requires a halo that is better resolved at '$z = 1$' than for a spherical satellite in order to reach the best stability. This can be explained by the fact that a better resolved centrally concentrated region of the halo is able to inhibit the formation of non-axisymmetries (e.g. see Athanassoula, Lambert & Dehnen 2005).

In order to check the robustness of our choices of both number of particles and softenings, we have followed the suggestion by the referee and also simulated one of the '$z = 1$' experiments adopting the same mass and softening for stars in the satellite and in the host disc. Reassuringly we found practically no difference in the global properties of the final thick disc in comparison to our 'standard' choice of numerical parameters.

A2.3 Time-step

The time-step Δt has been defined for our simulations according to the standard criterion of GADGET-2.0. This means that the time-step for each particle is calculated as $\Delta t = \sqrt{2\eta\epsilon/|\boldsymbol{a}|}$, where η is a dimensionless parameter controlling the accuracy of the time-step criterion, ϵ is the softening associated to each particle and $\boldsymbol{a}$ is the gravitational acceleration suffered by each particle. Δt is also limited by a maximum value in order to prevent particles having too large time-steps. The maximum time-step is defined as a few per cent of the time-scale $t_c = 2\pi\epsilon/V_c(\epsilon)$ calculated for the component that has the smallest ϵ in the system, where V_c is the circular velocity.

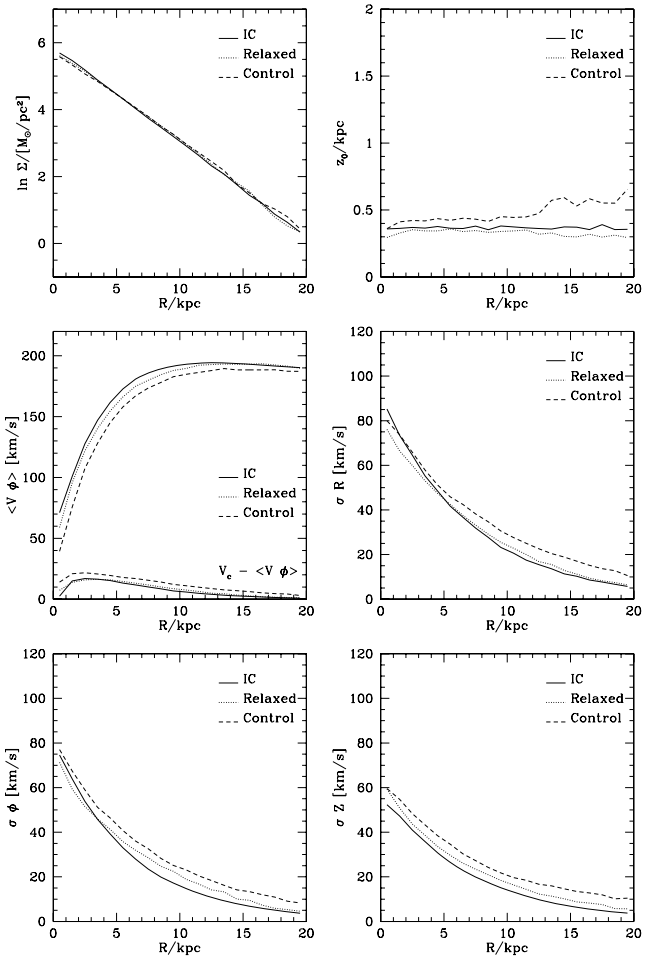

Figure A2. Evolution of the structural and kinematic properties of the isolated host disc, for the '$z = 0$' configuration. The solid lines show the initial conditions. The dotted lines show the disc after 1 Gyr of evolution within the fixed halo potential. The dashed lines show the disc's evolution after 5 Gyr within the *N*-body halo. The latter model is used as the control case in the comparison to the minor merger simulations. A similar behaviour is obtained for the disc in the '$z = 1$' configuration.

This ensures us that we follow the evolution of even the smallest components in the system with enough time resolution. We have set $\eta = 0.025$ and the maximum time-step to 0.25 Myr, which give us typical conservations of energy and angular momentum that are better than 0.1 per cent over 9 Gyr of evolution for our main disc galaxy configured at '$z = 0$'.

A3 Evolution of isolated host

To test the stability of the host galaxy, this is simulated in isolation, i.e. in the absence of any external perturbation.

We first relax the disc component within a 'rigid version' of the halo potential (which mimics the *N*-body halo described in Section A.1.1) for a few rotational periods (normally 1 Gyr). Once the disc component is relaxed (i.e. there are no further changes in either its morphological or kinematical properties) the 'rigid' halo is simply replaced by its *N*-body ('live') counterpart, and evolved for additional 5 Gyr in isolation for the configuration at '$z = 0$', and during 4 Gyr for that at '$z = 1$'. As described in Section 3.1, these time windows are enough to study the merger events that are

of interest to us. Strong bar instabilities appear in the host galaxies evolved in isolation only after 9 and 7 Gyr for the configurations at '$z = 0$' and '$z = 1$', respectively.

Fig. A2 shows how the initial properties of the host disc at '$z = 0$' change after being relaxed within a fixed halo for 1 Gyr, and after 5 Gyr in the live halo. Its properties are measured in concentric rings of 1 kpc of width, including particles out to $\sim$15 initial scaleheights. The surface density profiles $\Sigma(R)$ (top left-hand panel) indicate that the scalelengths of the discs (given by the inverse of the slope in log-linear scale) stay practically unchanged. Similarly, the vertical structure of the disc does not show significant evolution (top right-hand panel), except a moderate amount of flaring in the outer disc, which is due to spiral instabilities induced by swing-amplified Poisson noise in the disc. The scaleheights, measured at $R = 2.4R_{\rm D}$, change from $\mathcal{Z}_0 = 0.35$ to 0.41 kpc in the '$z = 0$' configuration and from 0.17 to 0.24 kpc in the '$z = 1$' one. The discs are also slightly slowed down (middle left-hand panel), while the velocity dispersions show an increase of $\sim$5 km s^{-1} in the first Gyr in the fixed halo, and a total of $<$10 km s^{-1} after 5 Gyr of evolution in the live potential (middle right-hand and bottom panels). The velocity ellipsoid of the disc (also measured at $R = 2.4R_{\rm D}$) increases from $(\sigma_R, \sigma_\phi, \sigma_z) = (28, 20, 17.5)$ to $(35, 28, 24)$ km s^{-1} in the '$z = 0$' configuration and from (25, 18, 14) to (32, 28, 22) km s^{-1} in the '$z = 1$' one.

This paper has been typeset from a TEX/LATEX file prepared by the author.